










ARTICLE

Cholesterol 25-hydroxylase mediates neuroinflammation and neurodegeneration in a mouse model of tauopathy

Danira Toral-Rios¹, Justin M. Long^{2,3,4}, Jason D. Ulrich^{2,3}, Jinsheng Yu⁵, Michael R. Strickland², Xianlin Han⁶, David M. Holtzman^{2,3,4}, Anil G. Cashikar^{1,2,3,7}, and Steven M. Paul^{1,2,3,7}

Alzheimer's disease (AD) is characterized by amyloid plaques and neurofibrillary tangles, in addition to neuroinflammation and changes in brain lipid metabolism. 25-Hydroxycholesterol (25-HC), a known modulator of both inflammation and lipid metabolism, is produced by cholesterol 25-hydroxylase encoded by *Ch25h* expressed as a "disease-associated microglia" signature gene. However, whether *Ch25h* influences tau-mediated neuroinflammation and neurodegeneration is unknown. Here, we show that in the absence of *Ch25h* and the resultant reduction in 25-HC, there is strikingly reduced age-dependent neurodegeneration and neuroinflammation in the hippocampus and entorhinal/piriform cortex of PS19 mice, which express the P301S mutant human tau transgene. Transcriptomic analyses of bulk hippocampal tissue and single nuclei revealed that *Ch25h* deficiency in PS19 mice strongly suppressed proinflammatory signaling in microglia. Our results suggest a key role for *Ch25h*/25-HC in potentiating proinflammatory signaling to promote tau-mediated neurodegeneration. *Ch25h* may represent a novel therapeutic target for primary tauopathies, AD, and other neuroinflammatory diseases.

Introduction

Alzheimer's disease (AD) is a progressive neurodegenerative disease histopathologically characterized by extracellular amyloid plaques containing aggregated forms of amyloid beta (A β)-peptides and intracellular neurofibrillary tangles composed mainly of hyperphosphorylated, aggregated tau. The onset and progression of tau pathology correlate with synaptic dysfunction and neuronal loss, leading to region-specific brain atrophy and cognitive impairment (Long and Holtzman, 2019). Neuroinflammation is a prominent neuropathological feature of AD, and considerable genetic and experimental evidence have implicated microglia, the brain's resident immune cell, as major drivers of innate immunity-induced neurodegeneration (Leyns and Holtzman, 2017). More than half of the reported genetic risk factors of AD are related to microglia-mediated immune response and cholesterol metabolism (Karch and Goate, 2015). Two of the major genetic risk factors for late-onset AD, apolipoprotein E (APOE) and the triggering receptor expressed on myeloid cells 2 (TREM2), are both highly expressed in a unique subset of

microglia, termed disease-associated microglia (DAM) (Keren-Shaul et al., 2017). A two-stage activation of microglial phenotype, switching from a homeostatic state to DAM, has been shown to be *ApoE* and *Trem2* dependent (Krasemann et al., 2017; Deczkowska et al., 2018; Keren-Shaul et al., 2017). Deficiency of *ApoE* or *Trem2* attenuates tau-dependent neuroinflammation and neurodegeneration in mice expressing human P301S mutant tau (PS19 mice) (Shi et al., 2017; Leyns et al., 2017; Sayed et al., 2018). In addition, pharmacological depletion of microglia in the same transgenic mice decreased the age-dependent progression of tau pathology, indicating that tau-dependent neurodegeneration may occur primarily as a result of microglial activation leading to a state of chronic neuroinflammation and subsequent neuronal cell death (Shi et al., 2019). Data also suggest that activated microglia may also secrete one or more factors leading to neurodegeneration (Leyns and Holtzman, 2017; Colonna and Butovsky, 2017).

Identification of the microglial factors that drive neuroinflammation-induced neurodegeneration is thus critically

¹Department of Psychiatry, Washington University School of Medicine, St Louis, MO, USA; ²Department of Neurology, Washington University School of Medicine, St Louis, MO, USA; ³Hope Center for Neurological Disorders, Washington University School of Medicine, St Louis, MO, USA; ⁴Knight Alzheimer Disease Research Center, Washington University School of Medicine, St Louis, MO, USA; ⁵Department of Genetics, Genome Technology Access Center at the McDonnell Genome Institute, Washington University School of Medicine, St Louis, MO, USA; ⁶Department of Medicine, Barshop Institute for Longevity and Aging Studies, University of Texas Health Science Center San Antonio, San Antonio, TX, USA; ⁷Taylor Family Institute for Innovative Psychiatric Research, Washington University School of Medicine, St Louis, MO, USA.

Correspondence to Anil G. Cashikar: cashikar@wustl.edu.

© 2024 Toral-Rios et al. This article is distributed under the terms of an Attribution–Noncommercial–Share Alike–No Mirror Sites license for the first six months after the publication date (see <http://www.rupress.org/terms/>). After six months it is available under a Creative Commons License (Attribution–Noncommercial–Share Alike 4.0 International license, as described at <https://creativecommons.org/licenses/by-nc-sa/4.0/>).

important and could lead to novel therapeutic strategies for treating or preventing AD and other tauopathies. In the current work, we focus on cholesterol 25-hydroxylase (Ch25h), which is upregulated in DAM only when both Apoe and Trem2 are present (Krasemann et al., 2017; Zhou et al., 2020). Ch25h converts cholesterol to 25-hydroxycholesterol (25-HC) (Lund et al., 1998). Mice lacking *Ch25h* appear to have a normal phenotype, show no changes in serum cytokine levels (Bauman et al., 2009), and have normal cholesterol metabolism (Reboldi et al., 2014). Ch25h is primarily expressed in myeloid cells under inflammatory conditions and has been shown to have several important immune-related functions involving both innate and adaptive immunity (Griffiths and Wang, 2022). *Ch25h* is an important interferon (IFN)-inducible gene, and 25-HC is believed to mediate the antiviral properties of IFN in response to infection with a variety of viral pathogens (Liu et al., 2013; Zu et al., 2020). 25-HC has also been reported to have both anti- (Reboldi et al., 2014; Dang et al., 2017) and proinflammatory (Gold et al., 2014; Fu et al., 2014) actions depending on the model system and context. In the central nervous system (CNS), *Ch25h* is upregulated in various mouse models of neuroinflammation (reviewed in The Myeloid Landscape 2 database reported in Friedman et al. [2018]). *Ch25h* was reported to be upregulated in patient-derived cells of X-linked adrenoleukodystrophy, and administration of 25-HC into the corpus callosum of mice induced potent proinflammatory activation of microglia, NLRP3 inflammasome-mediated neuroinflammation, interleukin 1 beta (IL-1 β) secretion, and cell death (Jang et al., 2016). We previously reported that *CH25H* is upregulated in AD brain as well as mouse models of amyloid and tau pathology (Wong et al., 2020). We further demonstrated that mouse primary microglia treated with the TLR4 agonist lipopolysaccharide (LPS) produces 25-HC that markedly augment IL-1 β production in an ApoE isoform-dependent manner (E4 >> E3 > E2) (Wong et al., 2020). Based on these findings, we hypothesized that 25-HC acts as a proinflammatory mediator and thus may contribute to neuroinflammation and neurodegeneration, characteristic of various tauopathies including AD. To test this hypothesis, we generated Ch25h-deficient PS19 mice and showed that Ch25h deficiency markedly attenuates neurodegeneration as well as significantly reduces the associated microgliosis and astrogliosis. Further, transcriptomic studies revealed marked suppression of inflammatory pathways and restored sterol biosynthesis in PS19 mice lacking Ch25h, suggesting a major role for 25-HC in mediating changes in lipid metabolism, neuroinflammation, and neurodegeneration. As a non-essential DAM gene, Ch25h may also represent a novel therapeutic target for AD and related tauopathies.

Results

Expression of Ch25h in the brains of AD patients and PS19 mice

We previously reported increased expression of *CH25H* mRNA in the frontal cortex of AD patients as well as in mouse models of amyloid deposition and tau-mediated neurodegeneration (Wong et al., 2020). Although single-cell transcriptomic analysis identified *CH25H* as a marker of DAM in AD patients and transgenic

mouse models bearing amyloid pathology (Zhou et al., 2020; Krasemann et al., 2017; Keren-Shaul et al., 2017) or tau pathology (Friedman et al., 2018), cell-specific expression of the Ch25h protein had not been demonstrated in AD brain. Hence, we examined the localization of the Ch25h protein in relation to markers for microglia and astrocytes by immunostaining in the frontal cortex of AD brain tissues at Braak stages I-II and VI (Fig. 1, A-C; and Table S1). Immunostaining with AT8 antibody, which recognizes phosphorylated tau (p-tau) on serine 202 and threonine 205 (Ser202/Thr205), showed that Braak stage VI samples had higher levels of p-tau relative to Braak I-II stage samples, as expected (Fig. S1 A). *CH25H* expression was expected at both Braak stages since amyloid plaques are present in all the analyzed samples (Table S1) and amyloid triggers glia activation. However, the total volume of *CH25H* immunoreactivity was significantly increased ($P < 0.01$) in Braak VI stage brain sections (33,338 μm^3 , 95% confidence interval [CI] 24,997–41,678) compared with Braak I-II (15,047 μm^3 , 95% CI 3,117–26,977). To identify *CH25H* cell-specific expression, a colocalization volume was created from *CH25H* and IBA1 immunoreactivity, and *CH25H* and GFAP immunoreactivity. About 90% of Ch25h immunoreactivity was observed within IBA1-positive microglia (Fig. 1, A, B, and D) and <1% in GFAP-positive astrocytes (Fig. 1, A and E). Increased *CH25H* volume observed in microglia in the late stages of AD suggests that tau pathology and associated neurodegeneration can induce Ch25h expression. Related to this, we previously identified an increased expression of Ch25h in the cortex of 9.5-mo-old PS19 mice (Wong et al., 2020), a tauopathy mouse model that over-expresses human tau containing the P301S mutation that causes a familial form of frontotemporal dementia (Yoshiyama et al., 2007). Here, we conducted a *Ch25h* RNA in situ hybridization assay (RNAscope; Fig. 1 G) in combination with immunostaining for Iba1 in the hippocampus of 9.5-mo-old female PS19 (T) mouse and age-match wild type (WT). The specificity of the Ch25h probe for RNAscope was validated by comparing the *Ch25h* mRNA signal in brain sections from WT and mice deficient for *Ch25h* (CKO). A low level of background reactivity was observed in the CKO mouse tissue (Fig. S1 B), similar to that observed using the negative control assay (for *Bacillus subtilis* dihydrodipicolinate reductase gene) RNAscope probe in CKO mouse tissue (Fig. S1 C), and was probably related to autofluorescence displayed in aged-mouse brain tissue. However, the RNAscope method allowed us to detect increased *Ch25h* expression in the PS19 mouse brain (Fig. 1 G).

To investigate whether Ch25h affects tau-mediated neuroinflammation and neurodegeneration, we generated and aged PS19 female mice lacking Ch25h (TCKO), PS19 mice (T), Ch25h knock out (CKO), and WT mice. We quantified relative *Ch25h* mRNA levels by quantitative PCR (qPCR) in the hippocampus of tau transgenic and non-transgenic female mice at 6 (Fig. S1 D) and 9.5 mo (Fig. 1 F) of age. Although it has been reported that at 6 mo of age only synaptic dysfunction (but no neurodegeneration) is observed due to tau accumulation in neurons accompanied by an increase in gliosis (Yoshiyama et al., 2007), no significant changes in *Ch25h* mRNA levels were detected in T mice relative to aged-matched WT mice (Fig. S1 D). By 9.5 mo of

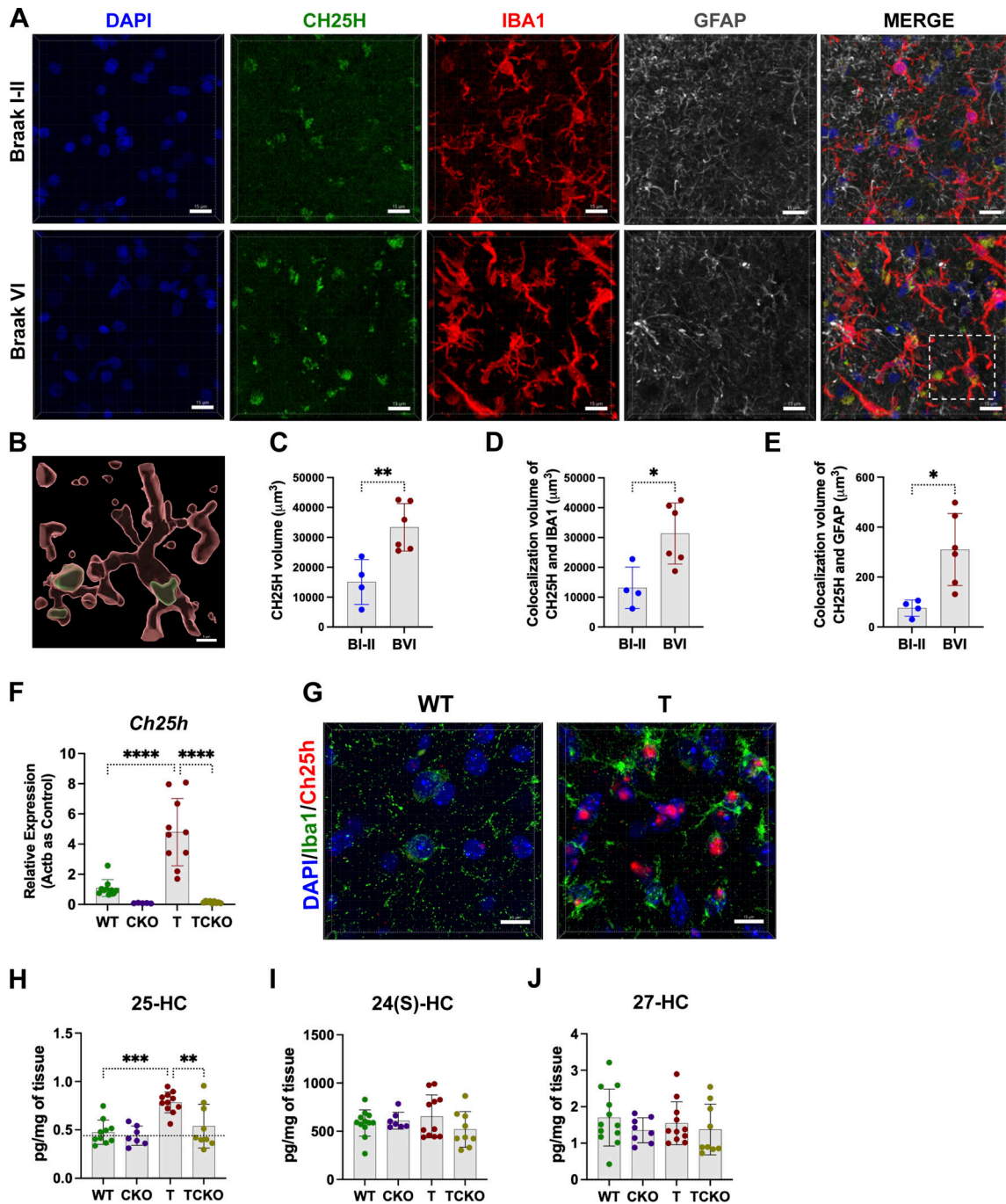


Figure 1. Ch25h is expressed mainly in microglia in brain tissue from AD patients and PS19 mice. (A) Representative images of Braak I–II and Braak VI stage frontal cortex sections stained with GFAP, IBA1, and CH25H (scale bar, 15 μ m). **(B)** A magnified surface 3D view of a single microglial cell (Braak VI) and CH25H surface is shown (scale bar, 5 μ m). **(C–E)** Total volume of CH25H immunoreactivity (C), colocalization volume of CH25H and IBA1-positive microglia (D), and colocalization volume of CH25H and GFAP-positive astrocytes (E) were quantified. **(F)** *Ch25h* mRNA relative levels were measured by qPCR in the hippocampus of WT ($n = 10$), CKO ($n = 5$), T ($n = 10$), and PS19 mice lacking Ch25h (TCKO, $n = 10$) mice. Gene expression was normalized with β -actin (Actb). **(G)** Representative images (scale bar, 15 μ m) from the hippocampus of 9.5-mo-old female WT and PS19 (T) mouse stained with a *Ch25h* RNAscope assay, DAPI, and Iba1. **(H–J)** Levels of 25-HC (H), 24-hydroxycholesterol (I), and 27-hydroxycholesterol (J) were quantified in the hippocampus of 9.5-mo-old female WT ($n = 11$), CKO ($n = 7$), T ($n = 11$), and TCKO ($n = 9$) mice. Data are expressed as mean \pm SD; one-way ANOVA with Tukey’s post hoc test (two-sided) was used for all statistical analysis. * $P < 0.05$, ** $P < 0.01$, *** $P < 0.001$, **** $P < 0.0001$.

age, a stage when T mice show marked neuroinflammation and neurodegeneration, we identified a three to fourfold increase in *Ch25h* expression in T mice compared with controls ($P < 0.0001$), as well as the absence of *Ch25h* expression in KO mice. Several

transcriptomic studies have shown that *Ch25h* is primarily expressed by microglia in the CNS (Friedman et al., 2018). Our previous studies with primary microglia isolated from WT and Ch25h-deficient mice show that only WT microglia produce and

secrete high levels of 25-HC upon stimulation with an inflammatory challenge, such as LPS (Wong et al., 2020). However, we cannot exclude the possibility that other cells such as astrocytes (Zhu et al., 2019) and oligodendrocytes (Jang et al., 2016) can express *Ch25h* in the context of inflammation or other disease-related pathology. However, our results suggest that *Ch25h* is mainly expressed in activated microglia in the brains of AD and PS19 mice.

To confirm that changes in *Ch25h* expression resulted in an increase in 25-HC synthesis, levels of 25-HC were quantified by liquid chromatography-mass spectrometry (LC/MS) in the hippocampus of mice at the same ages (Fig. 1 H and Fig. S1 E). Consistent with the expression of *Ch25h*, a significant increase ($P < 0.0001$) in the amount of 25-HC was observed only in T mice by 9.5 mo of age compared with WT mice (Fig. 1 H). The low levels of 25-HC observed in the brain tissue of all mice other than T mice may be produced by other cytochrome P450 enzymes (CYP3A4, CYP27A1, and CYP46A1) or via non-enzymatic oxidation (Smith, 1987). Levels of two oxysterol isomers of 25-HC, namely, 24S-hydroxycholesterol (24S-HC) and 27-hydroxycholesterol (27-HC), were also measured at 9.5-mo-old (Fig. 1, I and J) and 6-mo-old mice (Fig. S1, F and G). Although both 24S-HC and 27-HC are produced in the CNS, they were unaffected by tau pathology. Taken together, our results indicate that *Ch25h* expression and 25-HC synthesis in microglia in the brains of P301S mice increase after the onset of tau pathology and are associated with neuroinflammation and neurodegeneration.

Ch25h deficiency blocks tau-mediated neurodegeneration in PS19 mice

PS19 mice develop a profound loss of neurons in the hippocampus and entorhinal cortex by 9 mo of age, accompanied by tau hyperphosphorylation and aggregation, neurofibrillary tangle formation, and gliosis (Yoshiyama et al., 2007). To determine whether *Ch25h* influences tau-mediated neurodegeneration in PS19 mice, we measured regional brain volumes in WT, CKO, T, and TCKO mice (Fig. 2 A). As expected, T mice developed marked brain atrophy primarily of the hippocampus and entorhinal/piriform cortex compared with WT and CKO mice (Fig. 2, B and C), while there was a trend for increased ventricular volume that was not statistically significant ($P = 0.226$) (Fig. 2 D).

A comparison of hippocampal volumes in WT (8.301 mm³, 95% CI 7.559–9.043), T (5.605 mm³, 95% CI 4.971–6.239), and TCKO (7.466 mm³, 95% CI 6.880–8.052) mice indicates that hippocampal atrophy in TCKO mice was reduced ($P < 0.001$) compared with T mice by ~70% (the percentage was calculated with the formula [(TCKO - T)/(WT - T)] × 100). Similar calculations in the entorhinal cortex reveal a reduction in brain atrophy in TCKO mice relative to T mice ($P < 0.001$) by 62%.

Next, we assessed neuronal loss by measuring the thickness of the pyramidal cell layer in the hippocampal CA1 region (Fig. 2 E), the granule cell layer (Fig. S2 A) of the dentate gyrus (DG), as well of the pyramidal cell layer of the piriform cortex (Fig. S2 D). Similar to what we observed for hippocampal and cortical atrophy, there was a significant loss of neurons in the granule (Fig. S2 B) and pyramidal cell layers (Fig. 2 F and Fig. S2 E) in T mice related to the control (WT) group. Neuronal loss in TCKO mice

was markedly reduced ($\geq 80\%$) and was similar to the non-transgenic control group. The comparison of CA1 pyramidal layer thickness in WT (68.38 μm , 95% CI 58.84–77.92), T (45.76 μm , 95% CI 41.48–50.04) and TCKO (60.33 μm , 95% CI 56.65–64.00) mice indicates that neuronal loss in TCKO mice relative to T mice was reduced ($P < 0.001$) by ~64% (Fig. 2 F). The percent reduction in neuronal loss observed for the DG granular layer and the pyramidal layer of the piriform cortex was 55% (Fig. S2 B) and 80%, respectively (Fig. S2 E). Changes in CA1 layer thickness correlated highly with hippocampal volumes (Fig. 2 G; correlation coefficient = 0.39, $P < 0.0001$), as did DG layer thickness (Fig. S2 C; correlation coefficient = 0.37, $P < 0.0001$), and the pyramidal layer of the piriform cortex thickness correlated with piriform/entorhinal cortex volume (Fig. S2 F; correlation coefficient = 0.58, $P < 0.0001$).

The synaptic loss was evaluated in the stratum lucidum of the hippocampal CA3 region by immunostaining for the presynaptic protein synapsin (Fig. 2 H and Fig. S2 G). A marked reduction of synapsin immunoreactivity was found in T and TCKO mice compared with WT mice (Fig. 2 I and Fig. S2 G). However, synapsin loss was significantly attenuated in TCKO mice relative to T mice ($P < 0.001$). The progression of tau pathology has been correlated with memory dysfunction and cognitive impairments in AD (DeVos et al., 2018; Giannakopoulos et al., 2003). In PS19 mice, early intracellular aggregation of tau can impair long-term potentiation, a mechanism related to synaptic plasticity and consolidation of memory (Yoshiyama et al., 2007). Soluble factors secreted by activated microglia under conditions of chronic inflammation have been thought to mediate aberrant synaptic phagocytosis inducing synapse loss and cognitive impairment (Butler et al., 2021; Dejanovic et al., 2018). Related to this, we recently demonstrated that 25-HC disrupts synaptic plasticity and learning in mice treated with LPS (Izumi et al., 2021), suggesting the possibility that 25-HC may trigger tau-induced impairment of synaptic plasticity in addition to neuronal loss. Nonetheless, the striking reduction in brain atrophy, and neuronal and synaptic loss in TCKO mice underscores an important role for *Ch25h* and 25-HC in the development of tau-mediated neurodegeneration.

Ch25h deficiency reduces tau phosphorylation and aggregation in PS19 mice but does not affect tau seeding and spreading

To determine whether the reduced neurodegeneration in TCKO mice was accompanied by a reduction in tau phosphorylation, we stained tissue sections with the AT8 antibody. As expected, p-tau was undetectable in WT and CKO mice and detected only in T and TCKO, which overexpressed human-mutant tau (Fig. 3 A). Quantification of the percentage of area covered by AT8 immunoreactivity revealed a significant decrease in AT8-positive p-tau in T mice lacking *Ch25h* in both the hippocampus and entorhinal/piriform cortex (Fig. 3, C and D). The comparison of the percentage of AT8 immunoreactive area in the hippocampus of WT (0.002%, 95% CI 0.001–0.004), T (19.59%, 95% CI 14.0–25.17), and TCKO (7.97%, 95% CI 5.404–10.52) mice indicates that AT8 immunoreactivity in TCKO mice was reduced ($P < 0.001$) compared with T mice by ~60%. The AT8

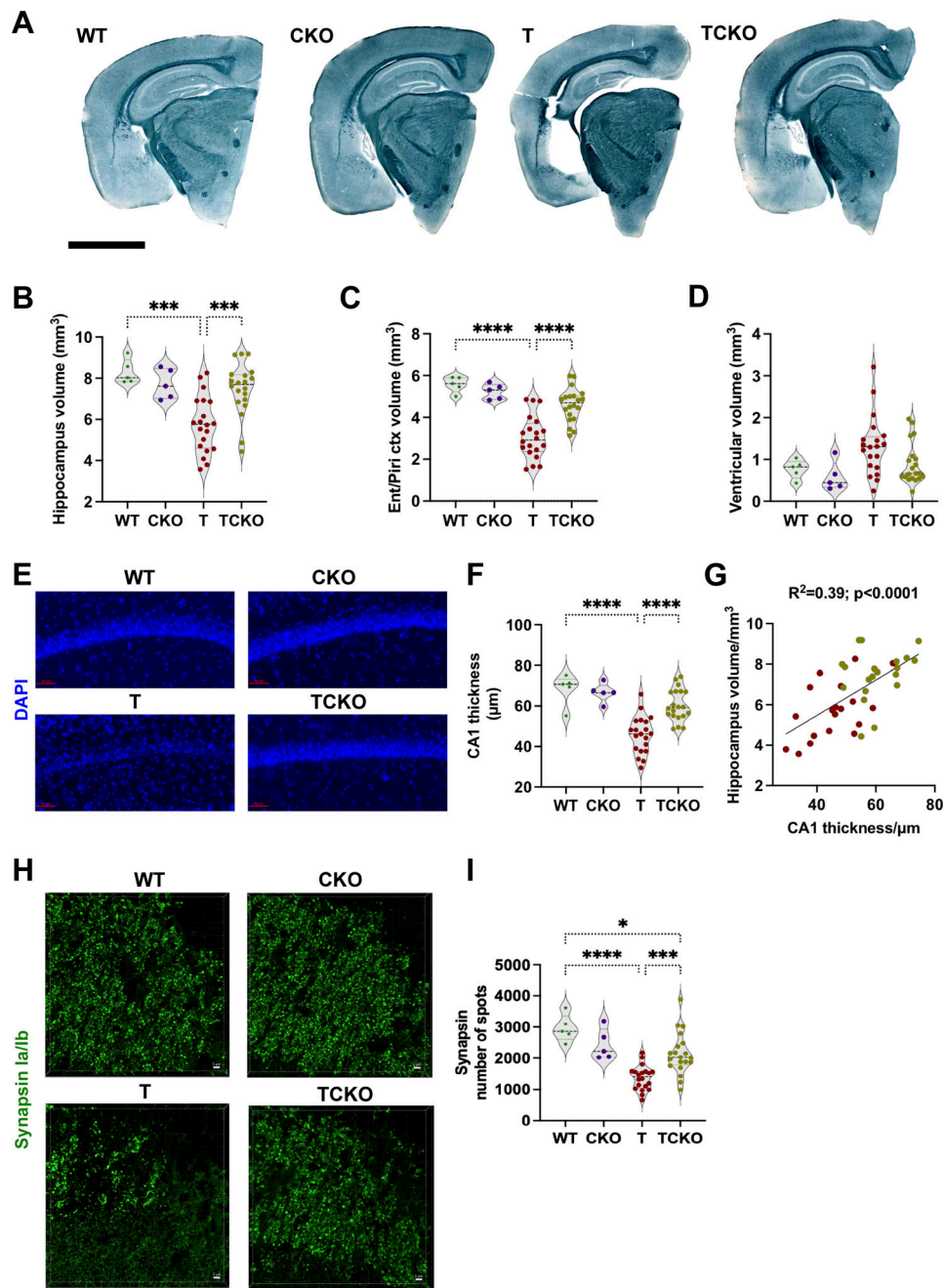


Figure 2. Ch25h deficiency reduces brain atrophy and neuronal loss in PS19 mice. (A) Representative images (scale bar, 2.5 mm) of 9.5-mo-old WT ($n = 5$), CKO ($n = 5$), PS19 (T, $n = 20$), and PS19/Ch25h KO (TCKO, $n = 20$) mouse brain sections stained with Sudan black (averaged data from three sections per mouse). (B–D) Brain volume analysis of the hippocampus (B), piriform/entorhinal cortex (C), and posterior lateral ventricle (D). (E and F) Representative images of mouse brain sections of the CA1 region stained with DAPI (E) (scale bar, 50 μm). The thickness of the pyramidal cell layer is shown in F. (G) Pearson’s correlation analysis (two-sided) between CA1 cell layer thickness with the hippocampal volume is shown for tau mice—T (red) and TCKO (asparagus). (H) Representative images of mouse brain sections stained with synapsin Ia/Ib antibody in the CA3 region (stratum lucidum) of the hippocampus (scale bar, 5 μm). (I) Quantification of the percentage of area covered by synapsin immunoreactivity. Data are expressed as mean \pm SD; one-way ANOVA with Tukey’s post hoc test (two-sided) was used for all statistical analysis. * $P < 0.05$, *** $P < 0.001$, **** $P < 0.0001$.

immunoreactivity in the entorhinal/piriform cortex was reduced in TCKO mice ($P < 0.05$) in comparison with T mice by 45%.

Hyperphosphorylation of tau induces conformational changes that promote protein aggregation (Alonso et al., 2001). The conformational state of tau was analyzed by

immunostaining with the MC1 antibody (Jicha et al., 1997), which recognizes aggregates in an early stage of AD (Fig. 3 B). The area covered by MC1 immunoreactivity (Fig. 3 E) was significantly higher ($P < 0.001$) in T mice (1.85%, 95% CI 1.152–2.564) relative to WT mice (0.03%, 95% CI 0.005–0.06). A significant reduction (75%) of MC1 immunoreactivity was

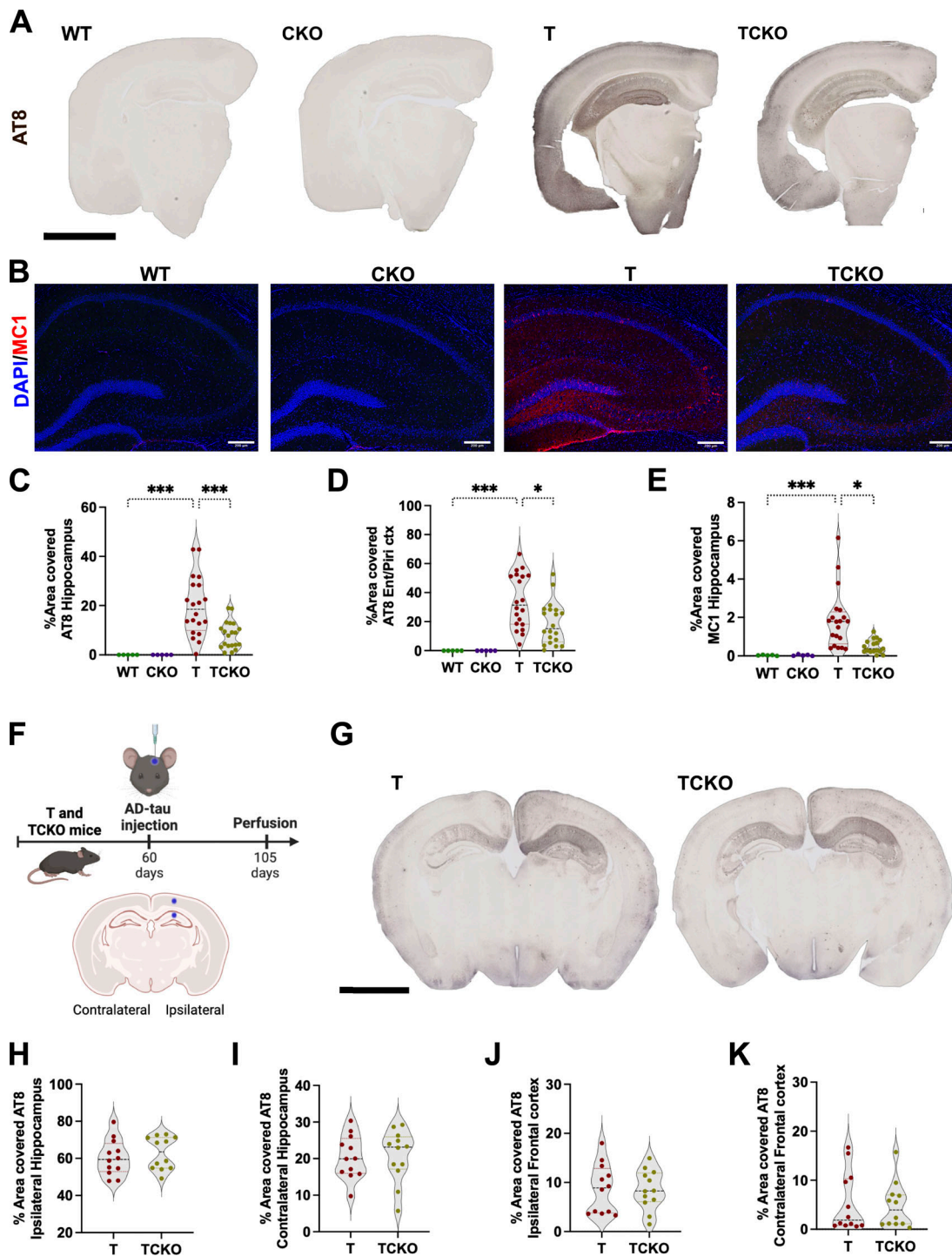


Figure 3. **Ch25h deficiency reduces p-tau (Ser202/Thr205) immunoreactivity and tau aggregation in PS19 mice.** (A) Representative images (scale bar, 2.5 mm) of 9.5-mo-old WT ($n = 5$), Ch25h KO (CKO, $n = 5$), PS19 (T, $n = 20$), and PS19/Ch25h KO (TCKO, $n = 20$) mouse brain sections stained with AT8 antibody (averaged data from three sections per mouse). (B) Representative images showing DAPI (blue) and MC1 immunoreactivity (red) in the hippocampus of 9.5-mo-old mouse brain sections (scale bar, 200 μm). (C and D) Quantification of the percentage of area covered with the AT8 immunoreactivity in the hippocampus (C) and entorhinal/piriform cortex (D). (E) The percentage of the area covered by MC1 immunoreactivity was quantified in the hippocampus. (F) Schematic of tau seeding and spreading model with intracerebral injections of AD-tau in T ($n = 12$) and TCKO ($n = 12$) mice. (G) Representative images (scale bar, 2.5 mm) from mouse brain sections immunostained with AT8 antibody. (H–K) Quantification of the percentage of area covered with AT8 immunoreactivity (average data from three sections per mouse) was performed in the ipsi and contralateral hippocampus (H and I), as well as ipsilateral and contralateral frontal cortex (J and K). Data are expressed as mean \pm SD; one-way ANOVA with Tukey's post hoc test (two-sided) was used for AT8 statistical analysis, and Kruskal–Wallis test for MC1. * $P < 0.05$, *** $P < 0.001$. Ent: entorhinal cortex, Piri: piriform cortex.

observed in TCKO mice (0.49%, 95% CI 0.310–0.672) compared with T mice. Our results suggest that Ch25h deficiency reduces tau phosphorylation and aggregation.

A protective role for 25-HC in blocking tau entry into neurons has been reported in a recent *in vitro* study (Tuck et al., 2022). To determine whether Ch25h deficiency affects tau seeding and spreading, we used the *in vivo* model described by Boluda et al. (2015), a model for tau seeding and spreading following intracerebral injection of AD brain extract enriched in pathological tau (AD-tau) in 2-mo-old T and TCKO mice (Fig. 3 F). This early age is prior to the onset of mutant tau transgene-induced pathology. Tau phosphorylation was evaluated by AT8 immunostaining in brain sections (Fig. 3 G). AD-tau injection induced abundant tau phosphorylation mainly in the ipsilateral hippocampus, where almost 60% of the area covered by AT8 immunoreactivity was detected and was similar in T and TCKO mice (Fig. 3 H). Only 8% of the ipsilateral frontal cortex area was covered by AT8 immunoreactivity and no significant changes between T and TCKO mice were observed (Fig. 3 J). Tau phosphorylation was detected in the contralateral hippocampus and frontal cortex (10% and 5% of the area covered by AT8 immunoreactivity respectively) equally in T and TCKO mice (Fig. 3, I and K). Our results indicate that under our *in vivo* assay conditions, Ch25h deficiency does not alter tau seeding and spreading.

Reduced gliosis in Ch25h-deficient PS19 mice

By 9.5 mo of age, PS19 mice manifested marked microgliosis and astrogliosis, which have been associated with tau phosphorylation and neurodegeneration (Yoshiyama et al., 2007; Shi et al., 2017). We have recently shown that 25-HC acts as an amplifier of the microglial inflammatory response (Wong et al., 2020) and can also regulate lipid metabolism in astrocytes (Cashikar et al., 2023). We hypothesized that 25-HC, produced by Ch25h-expressing microglia, exerts autocrine and paracrine effects contributing to tau-dependent neuroinflammation. To test this, we quantified markers of astrocyte and microglial activation and conducted an analysis of glial morphology. Sections immunostained for GFAP were assessed for astrogliosis (Fig. 4 A). A marked increase in the area covered by the GFAP immunoreactivity was observed in T mice compared with WT and CKO mice in the hippocampus ($P < 0.001$; Fig. 4 C) and entorhinal/piriform cortex ($P < 0.001$; Fig. 4 D). Although, the percentage of area covered by GFAP in TCKO mice was greater than that of non-tau mice (WT and CKO), the differences were not significant ($P < 0.1348$ and $P < 0.1460$). However, the area of GFAP immunoreactivity in TCKO brain tissue was significantly lower than that in T mice in the hippocampus ($P < 0.01$; Fig. 4 C) as well as entorhinal/piriform cortex ($P < 0.01$; Fig. 4 D). In the astrocyte morphology analysis (Fig. 4 B), we identified numerous reactive astrocytes in T mice, characterized by a significant reduction ($P < 0.00001$) in the length of the processes (Fig. 4 E) and the number of branches per cell (Fig. 4 F). Astrocytes from TCKO mice displayed a significant reduction in both parameters in comparison with WT mice, and the processes were more ramified than astrocytes in T mice ($P < 0.00001$), which is consistent with the reduction in GFAP immunoreactivity.

To assess microgliosis, we immunostained sections for Iba1 together with a cluster of differentiation 68 (CD68), a phagolysosome marker expressed by activated microglia (Fig. 4 G) (Hopperton et al., 2018). The area of Iba1 and CD68 immunoreactivity was significantly elevated in T mice in agreement with previously published results (Shi et al., 2017). The percentage of surface area covered by Iba1 immunoreactivity was markedly reduced in TCKO mice in comparison with T mice in the hippocampus ($P < 0.05$; Fig. 4 I) as well as in entorhinal/piriform cortex ($P < 0.0001$; Fig. 4 J). The area covered by CD68 immunoreactivity was also significantly reduced in the hippocampus ($P < 0.05$; Fig. 4 K) and entorhinal cortex ($P < 0.0001$; Fig. 4 L) of TCKO mice. No significant differences were detected in Iba1 and CD68 immunoreactivity between TCKO and non-tau (WT and CKO) mice. Homeostatic microglia present a ramified morphology with longer processes (Schwabensland et al., 2021), such as that observed in WT and CKO mice (Fig. 4, H, M, and N), while microglia from T mice display a hypertrophic morphology characterized by a significant reduction in process length and number of branches per cell ($P < 0.0001$). We found that microglia from TCKO mice also present a significant reduction in the number of branches per cell compared with the non-tau mice (Fig. 4 N), but the processes were in fact significantly longer ($P < 0.05$) than microglia from T mice (Fig. 4 M), which suggests microglia in TCKO mice are less activated, possibly in an intermediate state of activation. Taken together, these results confirm that Ch25h deficiency results in significantly reduced astrocyte and microglial reactivity in PS19 transgenic mice.

Ch25h deficiency reduces DAM in PS19 mice

Single-cell transcriptomic analysis carried out in AD human and AD mouse model brain tissue have identified unique signatures of gene expression in microglia in physical proximity to amyloid plaques and tau aggregates, termed DAM (Keren-Shaul et al., 2017; Krasemann et al., 2017; Zhou et al., 2020). This microglial subset is characterized by reduced expression of homeostatic genes (e.g., *Tmem119*, *P2ry12*, *Cx3cr1*) and increased expression of inflammatory genes (e.g., *Clec7a*, *ApoE*, *Trem2*) including Ch25h (Chen and Colonna, 2021). Given the decrease in microglial reactivity observed in TCKO mice, we further investigated whether Ch25h deficiency favors a reduction in DAM in lieu of a more homeostatic phenotype in T transgenic mice. To this end, we quantified *Clec7a* and *Tmem119* immunoreactivity in the hippocampus and entorhinal cortex of T versus TCKO mice. The area covered by *Clec7a* immunoreactivity (Fig. 5 A) was substantially decreased (approximately threefold, $P < 0.05$) in the hippocampus (Fig. 5 B) and entorhinal cortex of TCKO mice relative to T mice (Fig. 5 C). *Clec7a* mRNA levels in the hippocampus of TCKO mice were also reduced by twofold ($P < 0.01$) in comparison with T mice (Fig. 5 D). No significant changes in *Clec7a* immunoreactivity were observed between TCKO and non-tau control (WT or CKO) mice. These results suggest that Ch25h and 25-HC may contribute to the transition of homeostatic to DAM. We next quantified two additional DAM markers, ApoE (Fig. S3 A) and *Trem2* (Fig. S3 D). As expected, ApoE immunoreactivity in the hippocampus increased markedly in T mice in comparison with control mice ($P < 0.0265$). Strikingly,

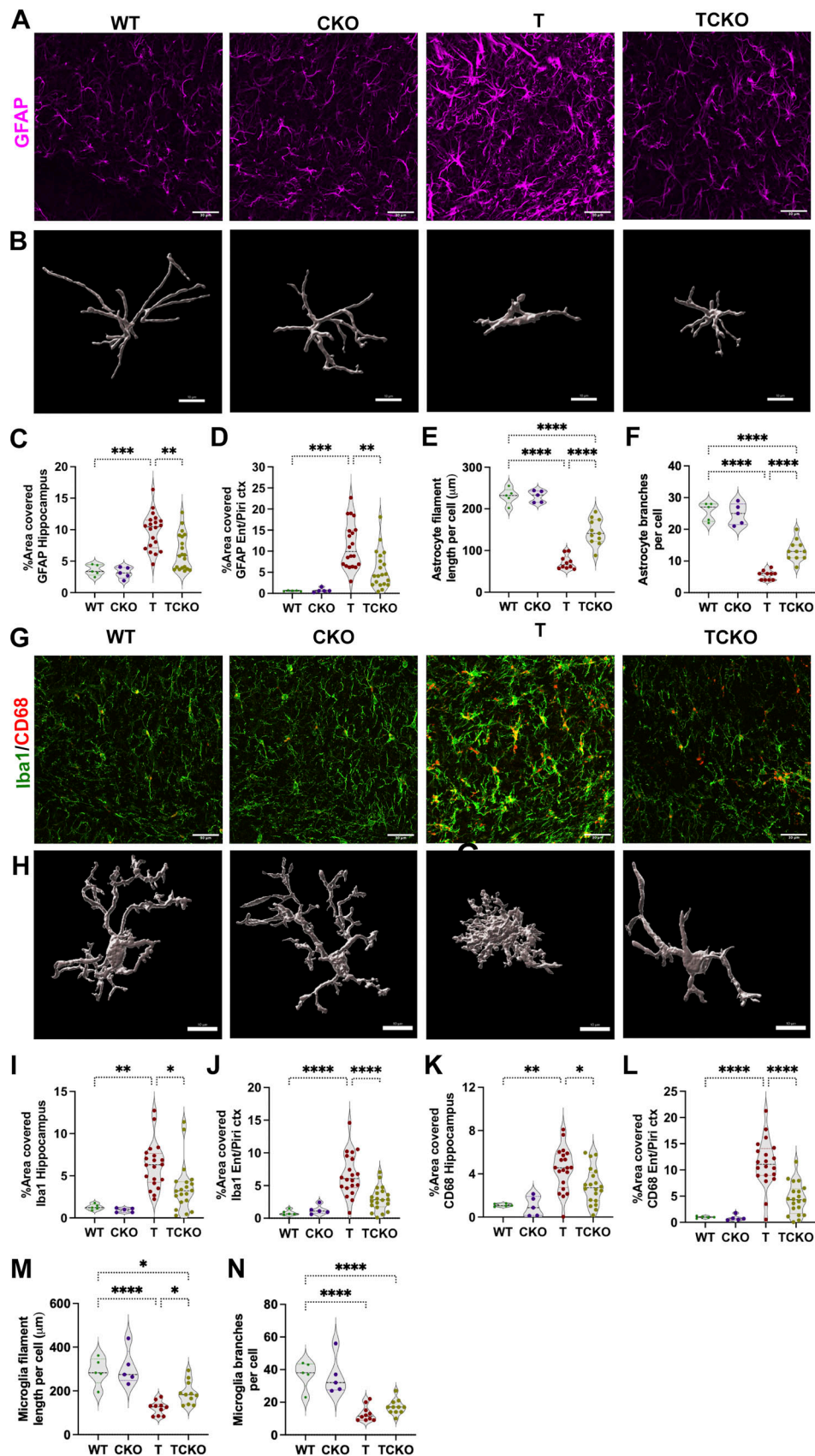


Figure 4. **Ch25h deficiency decreases gliosis in PS19 mice.** (A and B) Representative images of sections stained with (A) GFAP antibody (scale bar, 30 μm) and (B) Imaris-3D reconstruction (scale bar, 10 μm) from astrocyte morphology analysis to assess astrogliosis in 9.5-mo-old WT (*n* = 5), Ch25h KO (CKO *n* = 5), PS19 (T *n* = 20), and PS19/Ch25h KO (TCKO *n* = 20) mice. (C–F) Quantification of the percentage of area covered by GFAP immunoreactivity in the (C)

hippocampus and (D) entorhinal/piriform cortex. For astrocyte morphology analysis, the filament length (E) and number of branches (F) per cell were quantified. (G) Representative images of sections stained with Iba1 (green) and CD68 (red) to assess microgliosis (scale bar, 30 μ m). (H) Imaris-3D reconstruction from a representative Iba⁺ microglia per group (scale bar, 10 μ m). (I–L) Quantification of the percentage of area covered by Iba1 (I and J) and CD68 (K and L) immunoreactivity in the hippocampus (I and K) and entorhinal/piriform cortex (J and L). (M and N) Quantification of microglial filament length per cell (M) and branches per cells (N) are shown. Data are expressed as mean \pm SD; one-way ANOVA with Tukey's post hoc test (two-sided) was used for all statistical analysis. *P < 0.05, **P < 0.01, ***P < 0.001, ****P < 0.0001. Ent: entorhinal cortex, Piri: piriform cortex.

ApoE immunoreactivity reverted in TCKO mice (P < 0.0381) to almost control levels (Fig. S3 B). Given that ApoE is also normally expressed by astrocytes, sections were double-stained for Clec7a to specifically quantify the changes in ApoE immunoreactivity in activated microglia. Almost all the increased ApoE

immunoreactivity in T mice relative to WT mice (P < 0.0199) localized to Clec7a-positive microglia (Fig. S3 C). Trem2 immunoreactivity (Fig. S3 E) was also found reduced in the hippocampus of TCKO mice relative to T mice (P < 0.01). Likewise, Trem2 immunoreactivity in Clec7a-positive microglia was also

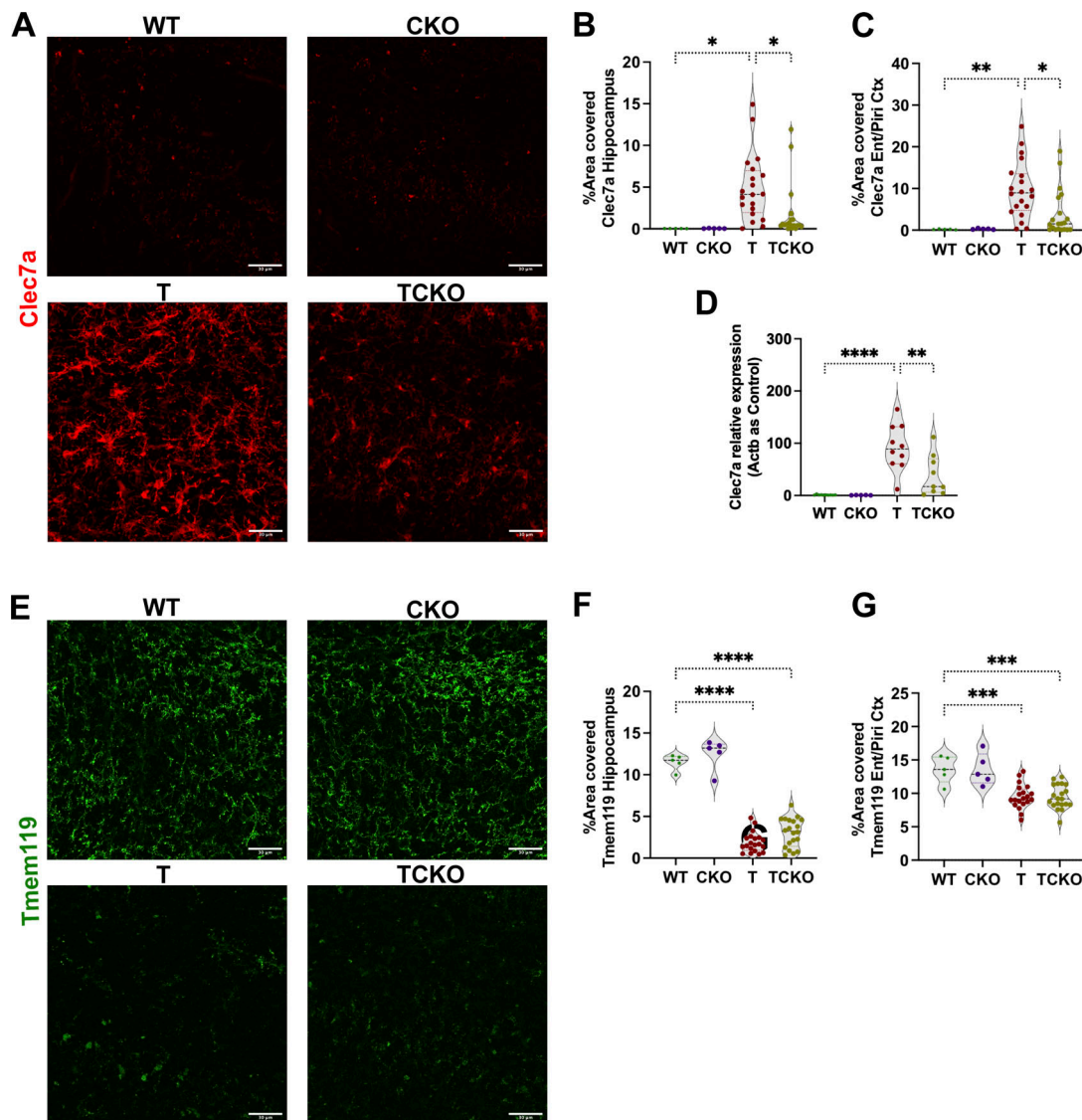


Figure 5. **Ch25h deficiency decreases DAM in PS19 mice.** (A) Representative images of DAM microglia stained with Clec7a antibody in 9.5-mo-old WT (n = 5), Ch25h KO (CKO, n = 5), PS19 (T, n = 20), and PS19/Ch25h KO (TCKO, n = 20) mouse brain sections. (B and C) Quantification of the percentage of area covered by Clec7a immunoreactivity in (B) hippocampus and (C) entorhinal/piriform cortex. (D) Relative expression of *Clec7a* mRNA in the hippocampus was quantified by qPCR (WT: n = 10, CKO: n = 5, T: n = 10, TCKO: n = 10). Gene expression was normalized with β -actin (Actb). (E) Representative images of homeostatic microglia immunostained for Tmem119. (F and G) Quantification of the percentage of area covered by Tmem119 in the (F) hippocampus and (G) entorhinal/piriform cortex. Data are expressed as mean \pm SD; one-way ANOVA with Tukey's post hoc test (two-sided) was used for all statistical analyses. *P < 0.05, **P < 0.01, ***P < 0.001, ****P < 0.0001. Scale bar, 30 μ m. Ent: entorhinal cortex, Piri: piriform cortex.

significantly decreased in TCKO relative to T mice ($P < 0.01$, Fig. S3 F).

Tau-mediated neuroinflammation also coincides with a marked decrease in homeostatic microglia (Sobue et al., 2021). To test whether the decreased activation of microglia in TCKO is also associated with a reversal to a more homeostatic (resting) state, we stained tissue sections for Tmem119 (Fig. 5 E). In T mice, the area covered by Tmem119 immunoreactivity was significantly reduced relative to control (WT and CKO) mice. Interestingly, the area covered by Tmem119 immunoreactivity remained reduced in TCKO mice in the hippocampus (Fig. 5 F; $P < 0.0749$) and entorhinal/piriform cortex (Fig. 5 G; $P < 0.9999$). This correlates with our findings from the morphological analysis, suggesting that microglia in TCKO mice only partially reverted back to the homeostatic state. To confirm these observations, we immunostained for an additional homeostatic microglia marker, P2ry12 (Fig. S3 G), and the total P2ry12 area was quantified (Fig. S3 H). Again, in T mice, P2ry12 area was markedly decreased similar to Tmem119. In TCKO mice, P2ry12 area also remained low and did not revert to control (WT and CKO) levels. Overall, Ch25h deficiency in T mice appears to strongly decrease the progression of reactive microglia to a DAM state, but without fully reverting to a resting (homeostatic) microglial state.

Ch25h deficiency results in transcriptomic changes involved in inflammation, cholesterol metabolism, and trans-synaptic signaling in PS19 mice

We next profiled the transcriptomic changes associated with Ch25h deficiency by RNA sequencing (RNA-seq) using RNA extracted from the hippocampus from WT, CKO, T, and TCKO mice ($n = 4$ mice per group). First, we compared the expression level of human transgenic *MAPT* gene in T and TCKO mice and found no significant differences, indicating that the prevention of neuroinflammation and neurodegeneration in TCKO was not simply due to reduced expression of the tau transgene compared with T mice. Differentially expressed genes (DEGs) filtered at $P < 0.05$ and fold change (FC) > 1.5 were analyzed for the following comparisons between groups: CKO versus WT, T versus WT, TCKO versus CKO, and TCKO versus T. The volcano plots (Fig. S4 A) show differentially up- and downregulated genes as well as the expression of *Ch25h*. The numbers of DEGs overlapping in different comparisons are shown in the Venn diagram (Fig. S4 B and C; and Table S2). In Fig. S4 D, we present a heatmap including all 3,918 DEGs between all four groups (gene lists are provided in Table S3). It is apparent that expression of the tau transgene results in increased expression of a large number of genes whereas only a smaller number of genes are downregulated in a tau-specific manner (Fig. S4 D). Interestingly, the tau-specific changes in gene expression were mostly absent in TCKO mice (Fig. S4 D). Some genes show increased or decreased expression in CKO and TCKO but not in WT and T mice (Fig. S4 D), suggesting that these DEGs are specifically changing due to the absence of Ch25h.

A comparison of DEGs between CKO and WT mice showed 295 upregulated genes and 305 downregulated genes (Fig. S4 A, B, and D; and Tables S2, S4, and S5). However, there were no

DEGs detected (up or down) when we corrected for false discovery rate (FDR; $q < 0.05$), highlighting the fact that Ch25h is not highly expressed under non-inflammatory conditions and thus deleting it did not cause major transcriptional changes under normal conditions (Table S2).

In contrast, the presence of the tau transgene caused a much greater number of DEGs on a *Ch25h*^{+/+} background than on the *Ch25h*^{-/-} background. In T versus WT comparison, 2,477 genes were upregulated and 831 were downregulated (Fig. S4, B and C). However, only 770 genes were upregulated and 275 were downregulated in TCKO compared with CKO mice, indicating that the tau transgene caused far fewer transcriptional changes in the absence of Ch25h. Further, comparing TCKO versus T mice, there were 459 genes that were upregulated and 1,634 genes that were downregulated relative to T mice (Fig. S4, C-G).

As expected, in T mice, important DAM signature genes including *ApoE*, *Trem2*, *Cst7*, *Clec7a*, *Tyrobp*, *Axl*, *Clq*, *Csfl*, *Cstd*, and *Cstb* were among those upregulated, while in TCKO mice, a marked reduction of DAM gene expression was observed (Fig. S4 H and Table S3). The upregulated reactive astrocyte genes in T mice including *Gfap*, *Aqp4*, *Vim*, *Id3*, *Fabp7*, *Mtl*, and *Mt2* were all decreased in TCKO mice (Fig. S4 I and Table S3). From this analysis, it is apparent that the DAM and reactive astrocyte gene expression profiles in TCKO mice are similar to WT and CKO mice.

We next performed a pathway enrichment analysis using Metascape, a bioinformatics tool that incorporates a core set of default gene ontologies (Zhou et al., 2019) (Fig. 6; and Tables S4 and S5).

Neuroinflammatory genes were not the only subset of genes impacted by Ch25h loss in T mice. Among the 831 DEGs that were downregulated in T versus WT mice, genes belonging to the gene ontology (GO) terms “trans-synaptic signaling,” “modulation of chemical synaptic transmission,” and “sterol biosynthesis” were also observed (Fig. 6, E and G; and Table S4). Upregulation of these same pathways was observed in TCKO versus T comparison (Fig. 6 B). Similar results were observed in the detailed heatmaps of individual DEGs belonging to the above pathways, where the gene expression levels were comparable with WT and CKO mice (Fig. S4, F and G). Analyses corresponding to the upregulated GO terms from the TCKO versus T dataset, namely “trans-synaptic signaling” (Fig. 6, E and F) and “sterol biosynthesis” (Fig. 6, G and H) revealed a single major subnetwork. In support of the observed DEGs in trans-synaptic signaling, we found that Ch25h deficiency prevented tau-mediated synaptic loss (Fig. 2, H and I).

GO analysis of the upregulated DEGs in T versus WT mice revealed pathways associated with inflammatory processes such as “regulation of cytokine production,” “leukocyte activation,” “regulation of defense response,” and “inflammatory response” (Fig. 6 A and Table S4). Analysis of the GO term “regulation of cytokine production” showed genes that were upregulated in a tau-specific manner in comparison to non-tau WT mice and were all downregulated in Ch25h-deficient PS19 mice (Fig. 6 C and Table S5). Interestingly, the heatmap corresponding to the same GO term indicates that the transcriptome of TCKO hippocampi was more similar to WT and CKO mice than to the

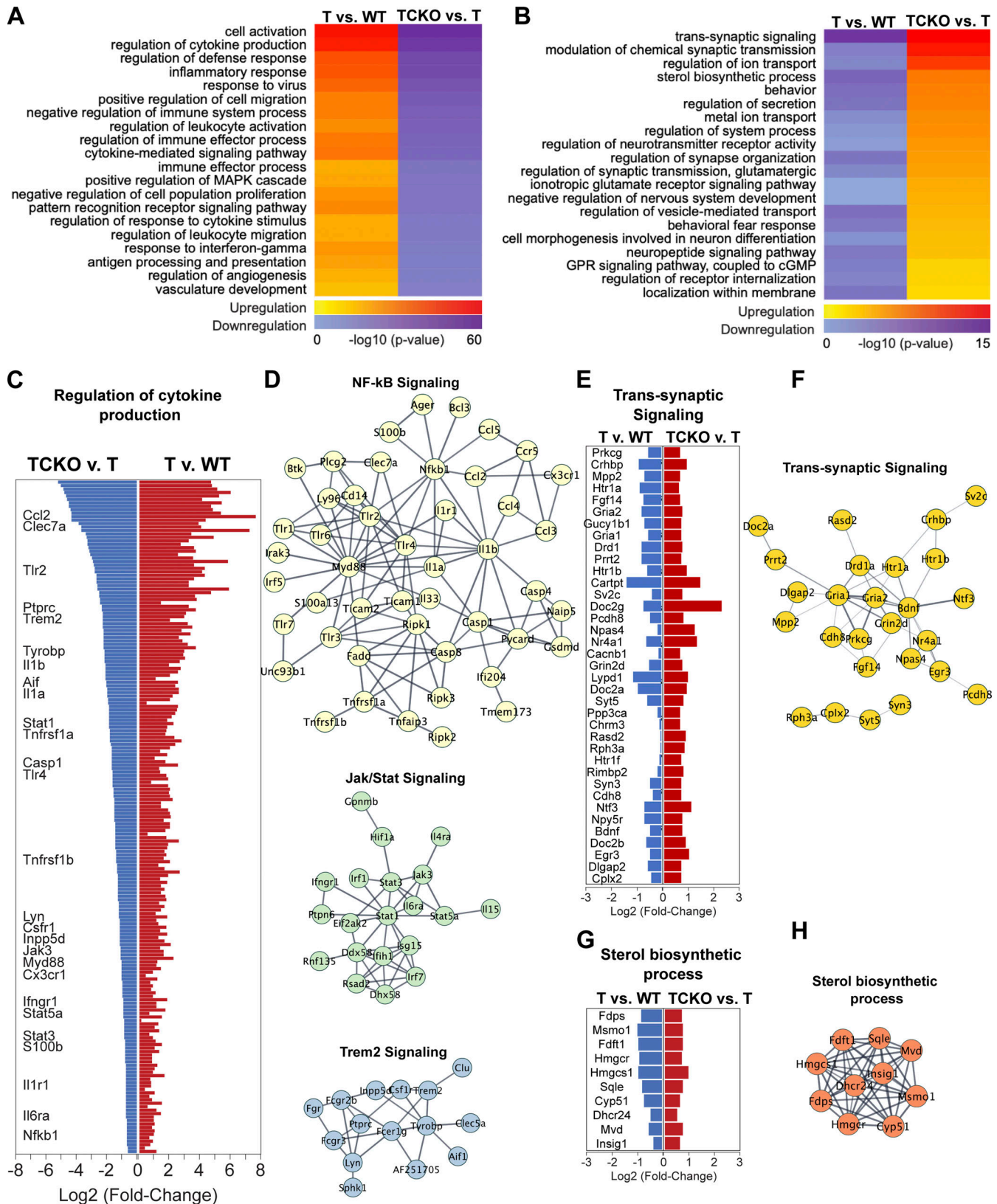


Figure 6. Ch25h deficiency results in the downregulation of DEGs related to inflammatory processes and upregulation of DEGs related to trans-synaptic signaling and sterol biosynthesis in tau transgenic mice. (A and B) Heatmaps of down- (A) and up- (B) regulated top GO terms in T versus WT and TCKO versus T comparisons and arranged based on P values from TCKO versus T mice comparisons in a decreasing order. (C–H) Shades of blue indicate downregulated GO terms, and shades of red indicate upregulated GO terms. Plots of \log_2FC in DEGs and interaction networks belonged to the GO terms “regulation of cytokine production” (C and D), “trans-synaptic signaling” (E and F), and “sterol biosynthetic process” (G and H) between T versus WT, and TCKO versus T mice comparisons.

transcriptome of T mice (Fig. S4 E). Remarkably, changes in the transcriptomic profile resulting from the expression of the mutant tau transgene were reversed in the absence of Ch25h despite the expression of the mutant tau transgene. Gene network analysis of the downregulated DEGs, corresponding to regulation of cytokine production from the TCKO versus T dataset, revealed pathways corresponding to “NF- κ B signaling,” “Jak/Stat signaling,” and “Trem2 signaling” (Fig. 6 D). This suggests an interplay between these proinflammatory pathways in tau-mediated neuroinflammation that is prevented by the absence of Ch25h.

We used the Transcriptional Regulatory Relationships Unraveled by Sentence-based Text mining (TRRUST) database (Han et al., 2015) to uncover the main transcription factors responsible for the differential expression of inflammatory pathway genes identified with bulk hippocampal tissue RNA-seq, focusing on genes upregulated in T versus WT comparison and downregulated in TCKO versus T comparison. Transcription factors such as *Rela* and *Nfkb1* (both from NF- κ B family), *Trp53*, *Sp1*, *Jun*, and *Stat3* were among the top drivers of the transcriptional differences observed between TCKO and T mice (Fig. 7 A).

Single nuclei transcriptomics reveals the cellular origins of transcriptional changes

To better understand and corroborate cell type-specific transcriptional changes associated with Ch25h deficiency in neuroinflammation in PS19 mice, we performed single nuclei RNA-seq (snRNA-seq) using hippocampal tissue (five mice pooled per group) from 6-mo-old T and TCKO mice, as well as 9.5-mo-old WT, T, and TCKO mice. Transcriptional data for 40,107 nuclei (Table S7) were subjected to unsupervised clustering into 16 distinct clusters (Fig. 8 A and Table S8) based on the expression of cell type-specific markers. The subclusters were categorized into excitatory neurons (exc 1,2,3,4,5,6,7), inhibitory neurons (inh 1,2,3), astrocytes (astro), microglia (micro), oligodendrocytes (oligo 1,2), oligodendrocyte precursor cells (opc), and choroid plexus epithelial cells (epi). Next, we examined the average expression of genes related to NF- κ B signaling, Jak/Stat signaling, and sterol biosynthesis for nuclei from specific cell type composition (Fig. 8 B). Genes related to NF- κ B and Jak/Stat pathways are highly expressed in microglia nuclei and genes related to sterol biosynthesis were highly expressed in astrocyte nuclei.

To understand how the inflammatory genes in microglia influence neurodegeneration, the microglia cluster was subclustered into five subclusters (cluster 0–4) of microglia in WT, T, and TCKO mice (Fig. 8, C and D; and Table S9). Most of the nuclei from our samples were grouped in cluster 0, identified by high mRNA expression of markers (e.g., *Cxcr3* and *P2ry12*) expressed in a microglia transcriptomic state commonly referred to as “homeostatic” (Fig. 8 D and Table S9) (Keren-Shaul et al., 2017). Microglia nuclei cluster 0 distribution in T and TCKO mice at 6-mo-old was comparable with 9.5-mo-old WT mice (Fig. 8, C and E). By 9.5 mo of age, however, a marked increase of nuclei from cluster 1 was identified in T and TCKO mice relative to WT (Fig. 8, C and E). Cluster 1 is characterized by high

expression of mRNA for markers (e.g., *Apobec*, *Apoe*, *Axl*, *Cd9*, and *Lpl*) typical of the transcriptomic signature referred to as microglial neurodegenerative (MGnD) or DAM (Fig. 8 D and Table S9) (Deczkowska et al., 2018; Keren-Shaul et al., 2017; Krasemann et al., 2017). An age-dependent increase of nuclei grouped in cluster 3 characterized by IFN signaling genes (e.g., *Stat1*, *Ifit2*) (Fig. 8 D and Table S9) was also observed in tau-transgenic mice compared to WT (Fig. 8, C and E).

Nuclei proportion analysis for each experimental group showed that the presence of tau pathology at 9.5 mo of age promoted a decrease in the percentage of nuclei of the homeostatic microglia (cluster 0) and an increase of DAM (cluster 1) and IFN (cluster 3) genes (Fig. 8 E and Table S10). Ch25h deficiency not only promoted an increase in the homeostatic microglia nuclei proportion but also decreased the DAM and the IFN subclusters (Fig. 8 E and Table S10). These results are in agreement with other data suggesting that the main effect of deleting *Ch25h* from tau transgenic mice is a reduction of microglial activation (specifically, DAM or MGnD).

Next, we examined how Ch25h deficiency alters the key pathways identified from bulk as well as single nuclei transcriptomics studies, namely (a) sterol and lipid metabolism, (b) NF- κ B and Jak/Stat signaling, and (c) leukocyte activation.

Ch25h deficiency in tau-transgenic mice reduces lipids associated with inflammation

To explore the impact of Ch25h deficiency in cholesterol and lipid metabolism, levels of desmosterol, free cholesterol, and other lipids were quantified in the cortex (Fig. S5). Although the bulk RNA-seq analysis in the hippocampus showed the downregulation of cholesterol biosynthetic enzymes in T mice respect WT mice that were restored in TCKO mice, levels of desmosterol (Fig. S5 A) and free cholesterol (Fig. S5 B) in the cortex were unaffected (T versus WT: desmosterol, $P < 0.6691$; free cholesterol, $P < 0.0794$). From our bulk lipidomic analysis (Table S6), several lipid classes were unchanged. However, we identified three subclusters (a–c) of lipids changing between WT, T, and TCKO mice (Fig. S5 C). In cluster a, we observed a significant reduction in the levels of different cardiolipins (CL) and lyso-cardiolipins species in T and TCKO mice relative to WT mice. CLs are a class of phospholipids that maintain stable mitochondrial membranes (Falabella et al., 2021). Reduced CL levels have also been observed in the triple transgenic AD mouse model (3xTg-AD), implicating oxidative stress and mitochondrial dysfunction (Monteiro-Cardoso et al., 2015). These changes, however, are unaffected by Ch25h loss. In cluster b, increased levels of three lyso-phosphatidylethanolamine species, as well as one species of phosphatidylcholine, lyso-phosphatidylcholine, and a cerebroside were detected in T and TCKO mice relative to WT mice. Decreased levels of phosphatidylethanolamine and phosphatidylcholine in AD brain tissue have been observed (Chew et al., 2020; Wood, 2012). The elevated levels of these lipids observed in T mice with or without Ch25h suggests that this is a tau-mediated phenomenon specific to PS19 mice which may not fully replicate all the lipid changes associated with AD. Cluster c was characterized by different species of cerebroside, sphingomyelin, phosphatidylinositol,

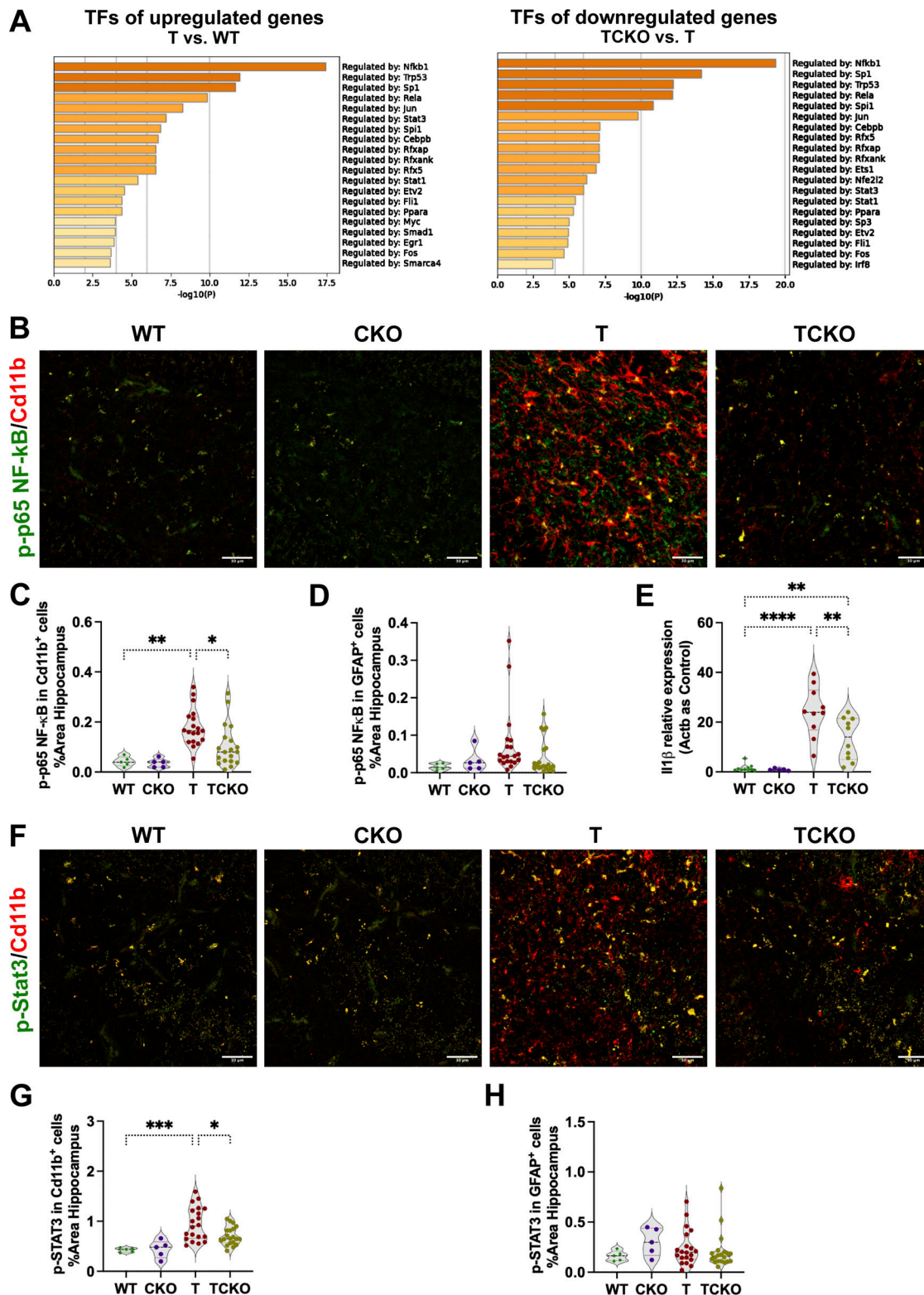


Figure 7. Ch25h deficiency in PS19 mice changes the expression of key transcription regulators of the inflammatory response. **(A)** TRRUST analysis of transcription factors (TFs) predicted to be responsible for the upregulated genes in T versus WT and downregulated genes in TCKO versus T comparisons. **(B)** Representative images from double immunostaining for p-p65 NF- κ B activated subunit (green) and the microglia marker Cd11b (red) in 9.5-mo-old WT ($n = 5$), Ch25h KO (CKO, $n = 5$), PS19 (T, $n = 19$), and PS19/Ch25h KO (TCKO, $n = 19$) mouse brain sections. **(C and D)** Quantification of the percentage of area covered by p-p65 NF- κ B immunoreactivity in Cd11b-positive cells (C) and in GFAP-positive cells (D) in the hippocampus. **(E)** Relative expression IL-1 β (*Il1b*) mRNA levels were quantified in the hippocampus by qPCR (WT: $n = 10$, CKO: $n = 5$, T: $n = 10$, TCKO: $n = 10$). Gene expression was normalized with β -actin (*Actb*). **(F)** Representative images from a double immunostaining for p-Stat3 (green) and the microglia marker Cd11b (red) in 9.5-mo-old WT ($n = 5$), Ch25h KO (CKO, $n = 5$), PS19 (T, $n = 20$), and PS19/Ch25h KO (TCKO, $n = 20$) mouse brain sections. **(G and H)** Quantification of the percentage of area covered by p-Stat3

ceramide, sulfatide, phosphatidylserine, and phosphatidic acid. Levels of lipids from this cluster were found significantly elevated in T mice compared with WT mice and strikingly downregulated in TCKO mice, suggesting that Ch25h deficiency may selectively alter lipid composition in the brains of tau-transgenic mice.

Activated microglia show activated NF- κ B and Jak/Stat signaling

Recent reports have indicated that the NF- κ B in activated microglia exacerbates neurodegeneration in PS19 mice (Wang et al., 2022). To extend our finding that two transcription factors of the NF- κ B family seemed to be differentially expressed in TCKO and T mice, we immunostained for phospho-p65 subunit of NF- κ B, an activated subunit of the NF- κ B transcription factor and the microglia marker Cd11b (Fig. 7 B). Consistent with the transcriptomics data, we found a dramatic increase in the area covered by p-p65 NF- κ B immunoreactivity within Cd11b-positive cells in the hippocampus of T compared with WT mice. Cd11b-specific p-p65 NF- κ B immunoreactivity was significantly decreased in TCKO mice relative to the T mice (Fig. 7 C). No differences were observed in the quantification of p-p65 NF- κ B immunoreactivity in GFAP-positive astrocytes (Fig. 7 D). Since the proinflammatory cytokine IL-1 β is a downstream target of NF- κ B (Greten et al., 2007), we also measured *Il1b* mRNA levels and observed a significant reduction in *Il1b* mRNA relative expression levels in TCKO mice in comparison with T mice (Fig. 7 E). We previously identified an augmented secretion of IL-1 β in mouse primary microglia treated with LPS which was attenuated in Ch25h-deficient microglia (Wong et al., 2020).

The signal transducer and activator of transcription 3 (Stat3) is a key regulator of the Jak/Stat signaling pathway and was markedly reduced in our bulk transcriptomic analysis (Fig. 6 C). A previous report showed that Stat3 is highly phosphorylated in activated microglia and exacerbates neurodegeneration in PS19 mice (Litvinchuk et al., 2018). Consequently, we immunostained for phosphorylated Stat3 (p-Stat3) and Cd11b in the hippocampus of WT, CKO, T, and TCKO mice (Fig. 7 F). Consistent with previous findings, p-Stat3 immunoreactivity was significantly increased in the microglia of T mice ($P < 0.0007$) and decreased in the microglia of TCKO mice ($P < 0.0176$) (Fig. 7 G). Immunoreactivity of p-Stat3 in astrocytes remained unchanged (Fig. 7 H). Taken together, our transcriptomic analyses of DEGs and identification of pathways altered by Ch25h deficiency strongly suggest that 25-HC is a critical positive modulator of neuroinflammation in PS19 mice.

Therefore, we examined if the reduced inflammatory response in microglia observed in tau-transgenic mice lacking *Ch25h* is reproducible in vitro in cultured primary microglia. To this end, we investigated the inflammatory response of mouse primary microglia from WT and CKO mice treated with preformed fibrils (0.5 μm) of human recombinant tau-441 (2N4R) P301S mutant protein (Fig. 9). First, we tested the ability of

Ch25h-deficient mouse primary microglia to phagocytose ATTO 488-conjugated preformed fibrils of P301S tau after 2 h of treatment (Fig. 9 A). Our results indicate that CKO and WT microglia phagocytose the tau fibrils similarly (Fig. 9 B), as a comparable amount of tau fibrils was found in CD68⁺ phagolysosomes in both cell types (Fig. 9 C). Next, we tested the effect of unlabeled preformed tau fibrils on the relative expression of genes related to inflammatory response in mouse primary microglia by qPCR. After 24 h of treatment, no changes in Ch25h expression (Fig. 9 D) were identified in WT mouse primary microglia treated with tau fibrils relative to the control. While tau fibrils induced the expression of *Il1b* (gene for IL-1 β ; $P < 0.01$) in WT microglia, a negligible increase was detected in CKO microglia (Fig. 9 E). However, tau fibrils did not alter the expression of *Tnf* (gene for TNF α) expression in either cell type (Fig. 9 F). Interestingly, CKO mouse primary microglia showed upregulated levels of expression of *Il10* (gene for the anti-inflammatory cytokine, IL-10) compared with WT mouse primary microglia ($P < 0.05$, Fig. 9 H). Furthermore, tau fibrils elicited increased expression of *Cxcl10* ($P < 0.01$) that was markedly reduced ($P < 0.05$) in CKO microglia treated with tau fibrils (Fig. 9 G). Similar suppression of *Cxcl10* expression in TCKO mice relative to T mice was observed by bulk transcriptomic analysis (Table S4). These in vitro data suggest that tau fibrils induce a proinflammatory response that is suppressed in the absence of Ch25h and 25-HC, similar to previous reports (Wong et al., 2020; Gold et al., 2014).

Ch25h deficiency reduces the T cell infiltration observed in PS19 mice

Infiltration of T cells mediated by DAM has been reported to play a crucial role in inducing neurodegeneration in PS19 mice (Chen et al., 2023). Pharmacological depletion of microglia reduced the number of T cells in the brain, and T cell depletion resulted in decreased neurodegeneration in T mice (Chen et al., 2023). Based on our bulk transcriptomic analysis of the hippocampus, genes clustered in the GO term "leukocyte activation" were found downregulated in TCKO mice compared with T mice. Considering the reduced microgliosis observed in TCKO mice, we immunostained mouse brain sections for the T cell-specific receptor, CD3 (Fig. 10 A). Consistent with the above-mentioned report (Chen et al., 2023), a significant increase in the percentage of area covered by CD3 immunoreactivity (Fig. 10 B) and number of CD3⁺ cells (Fig. 10 C) was found in the hippocampus of T mice compared with the controls ($P < 0.01$), as well as TCKO mice ($P < 0.05$). These results demonstrate that upregulation of Ch25h/25-HC may contribute to microglia-mediated T cell infiltration in the PS19 mouse model.

Discussion

In this study, we confirmed that by 9.5 mo of age, PS19 mice manifest significant tau accumulation, neuroinflammation

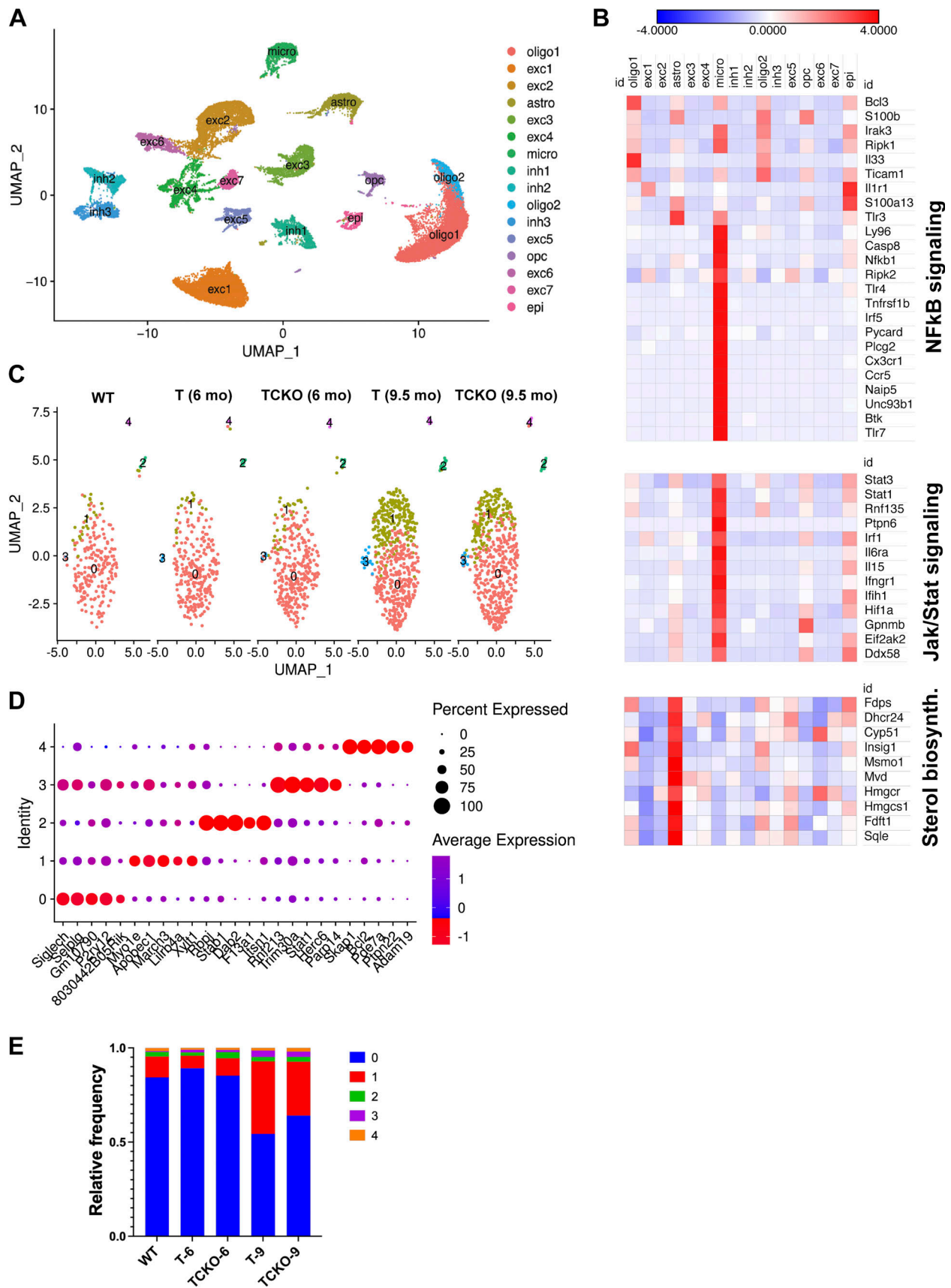


Figure 8. snRNA-seq reveals microglia-specific changes resulting from Ch25h deficiency in PS19 mice. (A) UMAP plot showing 16 distinguishable clusters (1–16) from snRNA-seq of hippocampal tissue from 9.5-mo-old male mice ($n = 5$ pooled per group) with corresponding cell types identified using

known cell markers (exc: excitatory neurons, inh: inhibitory neurons, astro: astrocytes, micro: microglia, oligo: oligodendrocytes, opc: oligodendrocyte precursor cells, epi: epithelial cells). **(B)** Average expression of genes related to NF- κ B signaling, JAK/STAT signaling and sterol biosynthesis in each cell type signature. **(C)** UMAP plot of the subclustered microglia population showing five distinguishable clusters (0–4) identified in WT (9.5-mo-old), T (6- and 9.5-mo-old), and TCKO mice (6- and 9.5-mo-old). **(D)** Dot plot showing the percentage of expression (dot size) and average gene expression levels (color intensity) of five of the most expressed specific markers in each microglia subcluster. **(E)** Relative frequency of microglia subclusters in each experimental group.

(microgliosis and astrogliosis), atrophy, and neuronal loss in the hippocampus and entorhinal/piriform cortex. We reported that all of these pathological hallmarks are markedly reduced in PS19 mice lacking *Ch25h*. We also confirm that *CH25H* is overexpressed by microglia in AD brain tissue as well as in the PS19 mouse model of tauopathy. We showed that increased expression of *Ch25h* and the concomitant increase in 25-HC levels in the brains of PS19 mice occur after 6 mo of age and may reflect exacerbated microglial activation. Interestingly, elevated levels of oxysterols including 25-HC were detected in late-stage AD brains (Testa et al., 2016). 25-HC is an oxysterol with potent immunomodulatory effects (Cyster et al., 2014). We and others have previously shown that *Ch25h* is responsible for the production and secretion of 25-HC by microglia (Bauman et al., 2009; Wong et al., 2020), and that microglia from *Ch25h* KO mice produce no detectable levels of 25-HC under basal conditions or when stimulated with LPS (Cashikar et al., 2023).

Several transcriptomic studies have also demonstrated that the expression of *Ch25h* is limited to microglia in the CNS (Friedman et al., 2018). Conversion of homeostatic microglia into DAM is a progressive change that occurs through a TREM2-independent stage (DAM1) followed by a Trem2-dependent stage (DAM2), characterized by increased expression of genes related to microglial phagocytic activity as well as lipid metabolism (e.g., *Ch25h*) (Keren-Shaul et al., 2017). Our results show that PS19 mice deficient in *Ch25h* and 25-HC have decreased expression of several DAM genes (e.g., *Apoe*, *Trem2*, and *Clec7a*) without fully restoring the homeostatic state of the cells. Thus, by simply eliminating one non-essential DAM gene, *Ch25h*, much of the neurodegeneration observed in aged PS19 mice was prevented similar to the effect observed by deleting *Trem2*, *Apoe*, or deleting microglia in PS19 mice (Leyns et al., 2017; Shi et al., 2017, 2019). Expression of *Ch25h* is controlled by Trem2 (Zhou et al., 2020; Poliani et al., 2015), and our transcriptomic results suggested that *Ch25h* may amplify Trem2 signaling, suggesting that 25-HC is a lipid effector that can modulate inflammatory functions of microglia. In agreement with a previous report (Kim et al., 2019), we identified an exaggerated inflammatory gene signature characterized by GO terms such as “positive regulation of cytokine production,” “leukocyte activation,” and “inflammatory response.” The absence of *Ch25h* in PS19 mice strikingly attenuated DEGs related to these same inflammatory pathways supporting a role for *Ch25h* in triggering neuroinflammation through 25-HC secreted by microglia, leading to age-dependent neurodegeneration. Specifically, in the context of regulation of cytokine production, NF- κ B signaling was among the top altered immune response pathways that potentially mediates the proinflammatory effects of 25-HC, and gene network analysis suggested a strong connection between NF- κ B pathway-related genes and IL-1 β production. Consistently, reduced phosphorylation

of p65 NF- κ B subunit and IL-1 β expression was observed in *Ch25h*-deficient PS19 mice. In a recent study by Jiang et al. (2021), p-tau was shown to induce IL-1 β expression through activation of the MyD88-NF- κ B pathway and NLRP3 inflammasome in a similar tauopathy mouse model (Jiang et al., 2021). Deletion of MyD88 or the inflammasome adaptor protein ASC in these mice blocked neuroinflammation, reduced p-tau levels, and improved cognition. In another recent report, inactivation of NF- κ B in microglia of PS19 mice partially restored microglial homeostasis, decreased tau seeding and spreading, and protected against spatial learning and memory deficits (Wang et al., 2022). We have previously shown that treatment of primary mouse microglia with the TLR4 agonist LPS markedly upregulates *Ch25h* expression and 25-HC secretion in addition to cytokine overproduction (Wong et al., 2020). Secretion of IL-1 β was augmented by 25-HC treatment of primary microglia and reduced in *Ch25h*-deficient microglia. 25-HC-mediated augmentation of IL-1 β secretion was due to enhanced caspase 1 activity via NLRP3 inflammasome activation (Wong et al., 2020). We corroborated that WT, but not *Ch25h*-deficient, mouse primary microglia stimulated by P301S tau fibrils express higher levels of IL-1 β mRNA. Moreover, *Ch25h*-deficient microglia express increased levels of the anti-inflammatory protein, IL-10, but decreased levels of the chemokine, Cxcl10. Cxcl10 is a key IFN- γ -inducible chemokine that has been previously reported to be stimulated by tau fibrils in mouse primary microglia (Udeochu et al., 2023), as well as in PS19 mice, where it may facilitate T cell infiltration into the brain (Chen et al., 2023).

T-lymphocyte infiltration into the brain has been previously reported in AD patients and has been associated with impaired cognition (Gate et al., 2020; Jorfi et al., 2023). Recent reports in two different mouse models of tauopathy (THY-tau22 and PS19 mice) suggest that exhausted activation of microglia is crucial to promoting the T cell infiltration into the brain, which exacerbates neuroinflammation and neurodegeneration and impairs cognition (Laurent et al., 2017; Chen et al., 2023). 25-HC is metabolized by *Cyp7b1* to 7 α ,25-dihydroxycholesterol, which is a high-affinity chemoattractant for leukocytes expressing the G-protein coupled receptor, *Gpr183* (also called *EBI2*) (Liu et al., 2011). Our finding of reduced T cells in the hippocampus of *Ch25h*-deficient PS19 mice may be due to decreased chemokine secretion from activated microglia (e.g., Cxcl10) and a lack of the well-characterized production of 7 α ,25-dihydroxycholesterol. In a mouse model of experimental autoimmune encephalomyelitis, expression of *Gpr183* was demonstrated in a variety of T cells and was shown to be required for the encephalitogenic T cell infiltration into the brain (Wanke et al., 2017). We speculate that in PS19 mice, increased expression of *Ch25h* results in increased 25-HC and 7 α ,25-dihydroxycholesterol production, leading to

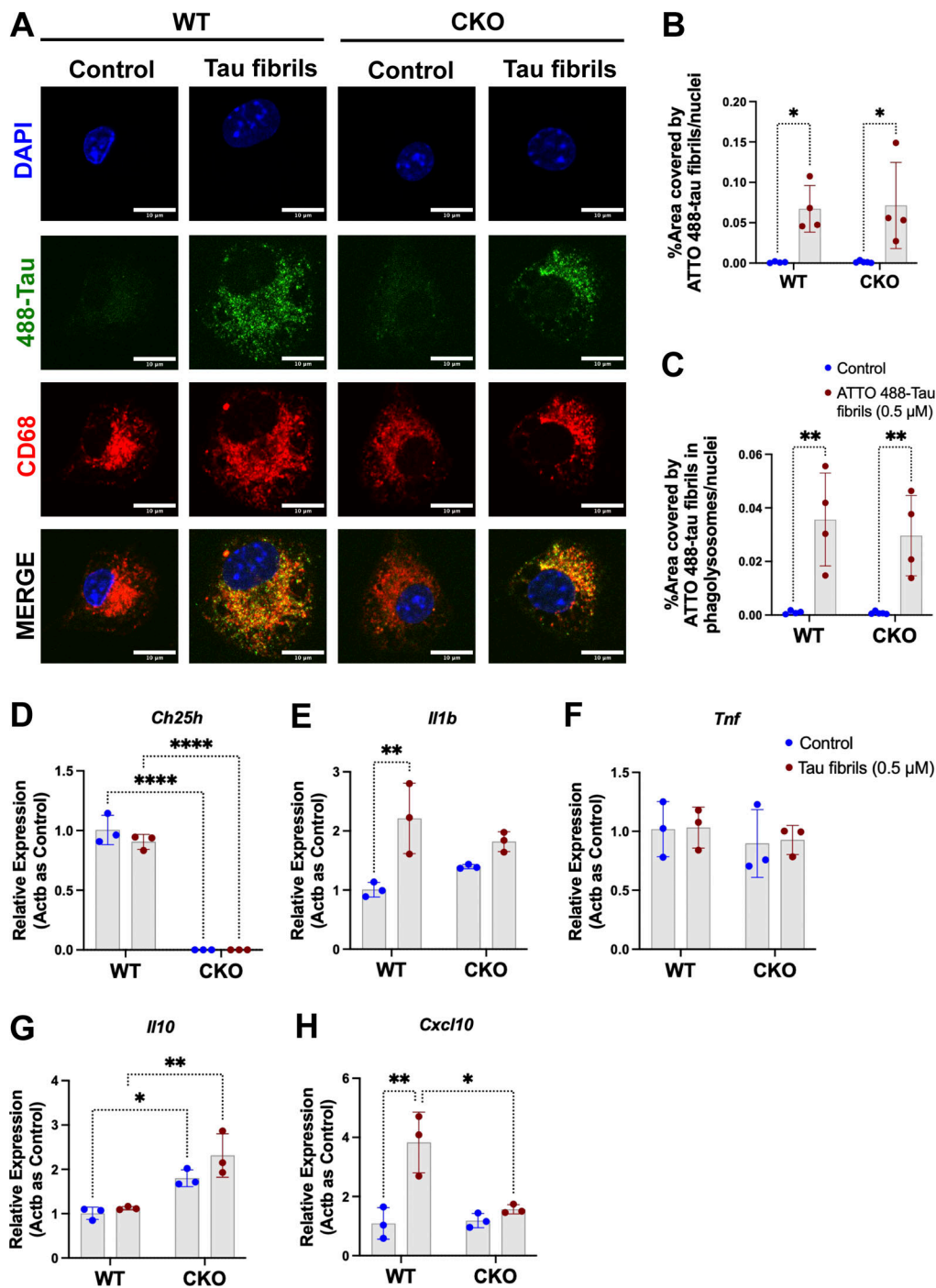


Figure 9. **Ch25h expression controls microglial inflammatory response induced by tau fibrils.** (A) Mouse primary microglia from WT and CKO mice were treated with vehicle or 0.5 μ M ATTO 488-conjugated tau preformed fibrils (green) for 2 h. Cells were costained with CD68 (red) and DAPI (blue). Phagocytosis of tau fibrils was evaluated by confocal microscopy (scale bar, 10 μ m). (B and C) Quantification of the percentage area of ATTO 488-conjugated tau fibrils (green) was conducted (B) as well as the localization in CD68⁺ phagolysosomes (C). Data were normalized to the number of nuclei. (D–H) Expression of *Ch25h* (D), *Il1b* (E), *Tnf* (F), *Il10* (G), and *Cxcl10* (H) was assessed by qPCR after 24 h of treatment of microglia with unlabeled tau preformed fibrils. Two independent experiments were conducted for tau uptake assay ($n = 4$) and microglia gene expression ($n = 3$). Two-way ANOVA with Tukey's post hoc test was used for the statistical analysis. * $P < 0.05$, ** $P < 0.01$, **** $P < 0.0001$.

increased CNS infiltration of leukocytes, further contributing to inflammation-induced neurodegeneration.

The fact that Ch25h-deficient PS19 mice also show less astrogliosis suggests that 25-HC secreted by microglia may contribute to the abnormal astrocyte function observed in neurodegenerative

disorders like AD. Among the genes expressed in astrocytes, loss of Ch25h restored the expression of sterol biosynthesis genes, which were significantly downregulated by tau pathology in PS19 mice. Downregulation of genes necessary for cholesterol biosynthesis in 7- and 9-mo-old PS19 mice has been recently

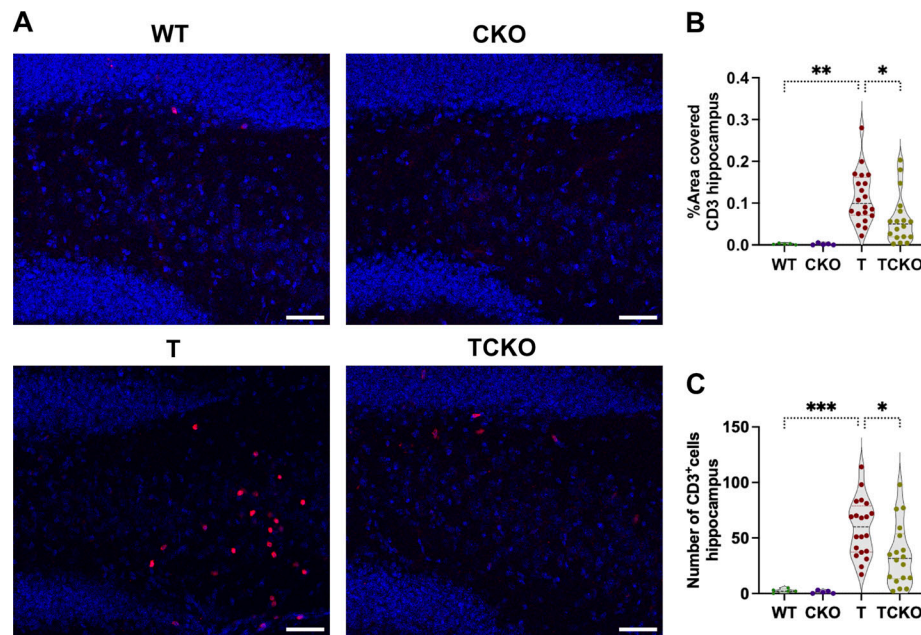


Figure 10. **Ch25h deficiency reduces brain T-cell infiltration in PS19 mice.** (A) Representative images of immunostaining of brain sections for the pan-T cell antigen, CD3 in the DG region costained with DAPI in 9.5-mo-old WT ($n = 5$), Ch25h KO (CKO, $n = 5$), PS19 (T, $n = 20$), and PS19/Ch25h KO (TCKO, $n = 20$). (B and C) Quantitation of the percent area covered by CD3 in each group (B) and quantitation of number of CD3⁺ cells found in the hippocampus (C). One-way ANOVA with Tukey's post hoc test (two-sided) was used for all statistical analyses. * $P < 0.05$, ** $P < 0.01$, *** $P < 0.001$. Scale bar, 50 μm .

reported (Tsumagari et al., 2022). Abnormal cholesterol metabolism has also been implicated in AD; however, both increased and decreased levels of cholesterol and its metabolites have been reported (Feringa and van der Kant, 2021; Sun et al., 2015; Di Paolo and Kim, 2011). Decreased expression of the cholesterol biosynthetic enzymes and the cholesterol biosynthetic intermediate, lanosterol, without significant changes in free cholesterol levels, has also been recently reported in AD brain tissue (Varma et al., 2021). In our study, we did not detect changes in free cholesterol or cholesterol precursors in the cortex of PS19 mice. Our snRNA-seq analysis shows however that the cholesterol biosynthetic enzymes are expressed mainly in astrocytes which are critical for cholesterol biosynthesis in the brain. The underlying mechanism by which 25-HC suppresses sterol biosynthesis genes likely involves its ability to inhibit the proteolytic processing of sterol response element-binding protein 2 (SREBP2), a master transcription factor that controls the transcription of genes encoding cholesterol biosynthetic enzymes (Radhakrishnan et al., 2007). We have recently shown that 25-HC inhibits cholesterol synthesis and promotes cholesterol esterification in primary mouse astrocytes (Cashikar et al., 2023). Interestingly, astrocyte-specific deletion of SREBP2 has been reported to markedly impair brain development, neuronal function, and behavior in mice (Ferris et al., 2017). A recent study using an in vitro model of tau entry into neurons showed that depletion of cholesterol from the plasma membrane or addition of 24(S)-HC promoted tau entry into the cytosol whereas 25-HC reduced it (Tuck et al., 2022). However, we did not detect any effect of Ch25h deficiency on tau seeding or spreading in vivo. Thus, we speculate that 25-HC inhibits SREBP2-mediated gene expression, leading to a suppression of cholesterol biosynthesis in

astrocytes, which in turn may contribute to the depletion of cholesterol in neurons, resulting in impaired neuronal function and possibly neurodegeneration in PS19 tauopathy mice.

Abnormal levels of various phospholipids and sphingolipids have also been reported in AD (Chew et al., 2020; Di Paolo and Kim, 2011; Wood, 2012; Akyol et al., 2021). Elevated levels of ceramides and galactosyl-ceramides have been reported in the middle frontal gyrus of AD patients (Cutler et al., 2004). In our study, increased levels of sphingomyelins, cerebroside (glucosyl- and galactosyl-ceramides) and ceramide were observed in PS19 mice suggesting a dysregulation of sphingolipid metabolism mediated by tau accumulation which was restored by the loss of Ch25h. Accumulation of ceramides in the brain can be stimulated by cytokines and oxidative stress, and ceramides can amplify neuroinflammation and promote apoptosis (Alessenko and Albi, 2020). It is tempting to speculate that the reduction in sphingolipids observed in Ch25h-deficient PS19 mice is related to the reduction in neuroinflammation and neurodegeneration.

Collectively, our data show that 25-HC produced by activated microglia contributes to tau-mediated neuroinflammation and neurodegeneration in PS19 mice. It will be important in future studies to assess the effects of 25-HC on behavior in PS19 mice. It is likely that 25-HC exerts synergistic effects with other cytokines and (or) chemokines as well as lipid mediators, resulting in age-dependent proinflammatory actions as well as recruitment of other immune cells into the brain. 25-HC may also elicit autocrine and paracrine effects to inhibit sterol biosynthesis necessary for normal neuronal function and viability. Thus, inhibitors of either Ch25h expression or enzyme activity may offer a novel strategy for reducing the

neuroinflammation and neurodegeneration that characterizes AD and other tauopathies.

Materials and methods

Animals

The PS19 transgenic mouse model overexpresses 1N4R human microtubule-associated protein tau (*MAPT*) driven by the PrP promoter, containing the P301S mutation that causes a familial form of frontotemporal dementia (Yoshiyama et al., 2007). PS19 tau transgenic mice (#008169; The Jackson Laboratory) were backcrossed and maintained on a C57BL/6 background. *Ch25h* KO mice (B6.129S6-*Ch25h^{tm1Rus}/J*) were purchased from The Jackson Laboratory (#016263). This strain was backcrossed to C57BL/6J for more than 10 generations by the donating laboratory. The PS19 (T) mice were crossed to the *Ch25h* KO (CKO) mice to generate WT, CKO, T, and TCKO mice. Only female mice were used for analysis in this study. All animal procedures and protocols were approved by the Institutional Animal Care and Use Committee at the Washington University School of Medicine.

Human AD tissues

All participants gave prospective pre-mortem written consent for their brain to be banked and used for research, with information to potentially be published under procedures approved by the human institutional review board at Banner Sun Health Research Institute.

Tissue collection

At 9.5 mo of age, mice were anesthetized with pentobarbital (i.p. 100 mg/kg) and sacrificed by cardiac perfusion with cold Dulbecco's PBS. The left hemisphere was collected and fixed in 4% paraformaldehyde (PFA) overnight before being transferred to 30% sucrose and stored at 4°C until they were sectioned coronally at 40 μm on a freezing sliding microtome (HM430; Thermo Fisher Scientific). Sections were stored in cryoprotectant solution at -20°C until use. The hippocampus and cortex were dissected from the right hemisphere and kept at -80°C until they were used for RNA isolation and biochemical analysis.

Volumetric analysis

Every sixth brain section (240 μm between sections) starting rostrally at -1.3 mm to the dorsal end of the hippocampus at bregma -2.8 mm was mounted on slides and allowed to dry overnight at room temperature. The following day, mounted sections were stained with 0.1% Sudan black in 70% ethanol at room temperature for 20 min, then washed in 70% ethanol three times for 1 min. The sections were rinsed in Milli-Q water and a coverslip was placed with Fluoromount-G (0100-01; Southern Biotech). Slides were imaged with the NanoZoomer 2.0-HT system (Hamamatsu Photonics). Hippocampus, posterior lateral ventricle, and entorhinal/piriform cortex areas were blinded to genotype and measured using the NDPview.2 software (Hamamatsu Photonics). The volume for each region of interest was calculated using the following formula: volume = (sum of areas) × 0.24 mm.

Neuronal layer thickness

Three sections (bregma -1.34, -2.3, -3.26 mm) per mouse were stained with DAPI (D1306; Invitrogen) and mounted with Fluoroshield. Images were acquired using the Zeiss Axio Scan 7 (Zeiss). The thickness of the CA1 pyramidal cell layer, DG granular cell layer, and pyramidal layer from the piriform cortex were blinded to genotype and measured by drawing a scale perpendicular to the cell layer at two spots in all three slices and taking the average value for each mouse using the Zen lite software (Zeiss).

Immunohistochemistry

Three sections (bregma -1.38, -2.34, -3.3 mm) per mouse were washed three times in TBS for 5 min and blocked in 0.3% hydrogen peroxide for 10 min. After washing, sections were blocked in 3% milk in TBS with 0.25% Triton X-100 (TBSX) for 30 min. AT8 primary antibody (mouse monoclonal-biotin, 1:500; MN1020B; Thermo Fisher Scientific) was diluted in 1% milk in TBSX, and the sections were incubated at 4°C overnight. The next day, sections were washed in TBS and incubated at room temperature in VECTASTAIN Elite ABC system (PK-6100; Vector Laboratories) for 1 h, followed by another washing step. Sections were developed in DAB solution (D5905; Sigma-Aldrich) for 10 min, washed, and mounted on slides. After drying overnight, the slides were dehydrated in increasing ethanol concentrations (from 50% to 100%) followed by xylene and coverslipped with Cytoseal 60 (8310; Thermo Fisher Scientific). Slides were scanned on the NanoZoomer 2.0-HT system. Images were processed and the AT8 percentage of area covered in the hippocampus and piriform/entorhinal cortex were quantified in the Fiji software version 2.3.0 using macro in batch mode.

Immunofluorescence

Free-floating sections (three per mouse, 960 μm apart from each other) were washed three times, 5 min each into 12-well plates with Netwell inserts (Corning) containing TBS. Tissues were blocked and permeabilized in 5% normal goat serum (NGS) and 3% bovine albumin serum (BSA) in TBSX for 1 h at room temperature (5% donkey serum in 0.5% TBSX for Trem2 immunofluorescence). Tissue was then incubated overnight at 4°C with primary antibodies CD68 (rat monoclonal, 1:400; MCA1957; Bio-Rad), Iba1 (rabbit polyclonal, 1:1000; 019-19741; FUJIFILM Wako's), GFAP (chicken polyclonal, 1:1,000; ab4674; Abcam), Clec7a or Dectin-1 (rat monoclonal, 1:100; mabg-mdect; Invivogen), Trem2 (sheep polyclonal, 1:400; AF1729; R&D Systems), ApoE (mouse monoclonal HJ6.3, 1:1,000; from D.M. Holtzman), Tmem119 (rabbit polyclonal, 1:250; 90840S; Cell Signaling), P2ry12 (rat monoclonal, 1:100; 848002; BioLegend), Cd11b (rat monoclonal, 1:400; 101202; BioLegend), p-STAT3 (rabbit polyclonal, 1:500; 9145S; Cell Signaling), p-p65 NF-κB (rabbit polyclonal, 1:3,000; 3033S; Cell Signaling), MC1 antibody (mouse monoclonal, 1:500; gift from the late Dr. Peter Davies, Albert Einstein College of Medicine, Bronx, NY, USA), CD3 (rat monoclonal, 1:500; 14-0032-82; Invitrogen). The following day, the sections were washed three times in TBS, followed by 1 h incubation at room temperature in secondary antibodies diluted in TBS (1:1,000; Invitrogen): goat anti-rabbit Alexa 488 (A32731),

goat anti-rat Alexa 555 (A21434), goat anti-mouse Alexa 647 (A32728), goat anti-mouse Alexa 555 (A32727), goat anti chicken Alexa 647 (A21449), donkey anti-sheep Alexa 555 (A21436), and donkey anti-rat Alexa 488 (A21208).

Sections were washed with TBS three times and mounted on Fisherbrand Superfrost Plus Microscope Slides (12-550-15; Thermo Fisher Scientific) and then coverslipped using Fluoroshield mounting medium. For quantification purposes, the hippocampus and entorhinal/piriform cortex were scanned in the Nikon Spinning Disk and analyzed with Fiji software version 2.3.0 using macro in batch mode. After analysis, representative images were acquired on an LSM 880 II (Zeiss) microscope. For P2ry12 quantification, a surface analysis was conducted using Imaris 9.5 software (Bitplane).

Glia morphology analysis

Three z-stacks (10 μm , 960 μm apart from each other) of GFAP and Iba1 immunostained sections were acquired on an LSM 880 II (Zeiss) with a 63 \times objective. Glia morphology was analyzed using the filament tracer in Imaris 9.5 software (Bitplane) as reported previously (Seo et al., 2023). The number of branch points and process length per cell were plotted. For microglia analysis the following settings were used: number of process lengths largest diameter 9.00 μm , seed points 2.200 μm ; remove seed points around starting points; and diameter of sphere regions: 15 μm . The following settings were applied for astrocyte morphology analysis: number of process lengths largest diameter 8.00 μm , seed points 2.000 μm ; remove seed points around starting points; and diameter of sphere regions: 8 μm .

Synaptic loss analysis

Immunofluorescence for synaptic markers Synapsin 1/2 (guinea pig polyclonal, 1:500; 106004; Synaptic Systems) and PSD95 (rabbit polyclonal, 1:200; 51-6900; Thermo Fisher Scientific) were performed as previously described (Gratuze et al., 2020) using the secondary antibodies goat anti-guinea pig Alexa 488 (1:1,000; A11073; Invitrogen) and goat anti-rabbit Alexa 594 (1:1,000; A11012; Invitrogen). Images were acquired at 63 \times in the stratum lucidum of the CA3 region on an LSM 880 microscope with AiryScan detector (Zeiss). A spot analysis was conducted in Imaris 9.5 software. Spots were detected using an automated background subtraction and spot settings detection for each channel (Synapsin spots: x - y size of 0.9 μm ; PSD95 spots: x - y size of 0.5 μm).

Immunofluorescence of human tissue

Human brain sections were obtained from the Banner Sun Health Institute. Demographic information is detailed in Table S1. For human tissue, 50- μm free-floating sections were washed in TBS followed by antigen retrieval performed with 10 mM sodium citrate buffer, pH 6, and 0.05% Tween at 60°C for 30 min. Sections were blocked with 5% goat serum in TBSX (0.5% Triton X-100). Antibodies were incubated in blocking solution at 37°C for 2 h: Iba (rabbit polyclonal), CH25H (mouse monoclonal, 1:150; from the hybridoma supernatant kindly provided by Dr. David Russell from UT Southwestern, Dallas, TX, USA), GFAP (chicken polyclonal), and anti-mouse biotin

AT8 (mouse monoclonal). For sections stained with AT8, we used Streptavidin Alexa 488 (1:500, S32354; Thermo Fisher Scientific). For the sections stained with IBA1, GFAP, and CH25H, we used the following secondary antibodies (1:1,000; Invitrogen): goat anti-chicken Alexa 488 (A11039), goat anti-rabbit Alexa 555 (A32732), and goat anti-mouse Alexa 647 (A32728). Three images (z-stacks 16 μm) per tissue were acquired on an LSM 880 microscope with at 20 \times magnification. 3D surfaces from CH25H, IBA1, and GFAP immunoreactivity were generated using a semiautomated pipeline based on MATLAB in Imaris 9.5 software (Bitplane). The total volume of CH25H was plotted. Next, surfaces of CH25H colocalizing with either IBA1 or GFAP surfaces were created, and the colocalization volume of CH25H and IBA1, and CH25H and GFAP was quantified.

RNAscope

RNAscope in situ hybridization assay was performed according to the manufacturer's instructions for fixed-frozen free-floating sections (Advance Cell Diagnostics [ACD]). Incubation was performed on the HybEz hybridization system (ACD). *Ch25h* mouse RNAscope probe was purchased from ACD (cat. no. 424561), as well as the negative (cat. no. 310043; ACD) and positive (cat. no. 313911; ACD) control probes. Detection was performed using RNAscope 2.5 HD Assay-RED. Following in situ hybridization, the sections were processed for immunofluorescence as briefly described using the rabbit anti-Iba-1 antibody with the corresponding goat anti-rabbit Alexa Fluor 488 secondary antibody. DAPI solution was added with the secondary antibody for counterstained nuclei. Images were acquired on an LSM 880 II (Zeiss) microscope and were processed similarly in Imaris 9.5 software (Bitplane).

RNA-seq and data analysis

Total RNA was isolated from mouse hippocampus with the Quick-RNA Miniprep Plus Kit (R1058; Zymo Research), and RNA integrity was determined using Agilent Bioanalyzer. The library was prepared with 10 ng of starting RNA with a Bioanalyzer RIN score >8.0. ds-cDNA was generated using the SMARTer Ultra Low RNA kit for Illumina Sequencing (Takara-Clontech) as per the manufacturer's protocol. cDNA was fragmented using a Covaris E220 sonicator using peak incident power 18, duty factor 20%, cycles per burst 50 for 120 s cDNA was blunt-ended, had an A base added to the 3' ends, and then had Illumina sequencing adapters ligated to the ends. Ligated fragments were then amplified for 12–15 cycles using primers incorporating unique dual index tags. Fragments were sequenced on an Illumina NovaSeq-6000 using paired-end reads extending to 150 bases. Basecalls and demultiplexing were performed with Illumina's bcl2fastq software and a custom python demultiplexing program with a maximum of one mismatch in the indexing read. RNA-seq reads were then aligned to the mouse genome (Ensembl release 76 primary assembly) along with an additional human *MAPT* gene with STAR version 2.5.1a1 (Dobin et al., 2013). Gene counts were derived from the number of uniquely aligned unambiguous reads by Subread:featureCount version 1.4.6-p52 (Liao et al., 2014).

All gene counts were then imported into the R package EdgeR (Robinson et al., 2010) where Trimmed Mean of M-values

(TMM) normalization size factors were calculated to adjust for samples for differences in library size. Ribosomal genes and genes not expressed in three samples with count-per-million >1 were excluded from further analysis. The TMM size factors and the matrix of counts were then fed into the R package Limma (Ritchie et al., 2015). Weighted likelihoods based on the observed mean-variance relationship of every gene and sample were then calculated for all samples with the voomWithQualityWeights (Liu et al., 2015). The performance of all genes was assessed with plots of the residual standard deviation of every gene to their average log-count with a robustly fitted trend line of the residuals. Differential expression analysis was then performed to analyze for differences between experimental groups, and the DEGs were defined as those with fold-change >1.5 at P value <0.05. The Benjamini-Hochberg FDR adjusted P values were also determined for further analysis.

Pathway enrichment analysis

Metascape (Zhou et al., 2019), a web-based gene annotation and biological enrichment tool that incorporates all major biological annotation databases including biological processes in GO terms, was utilized for pathway enrichment analysis. One of its key features was collapsing redundant biological terms with a similar set of DEGs into representative terms to help capture the most significantly enriched pathways. It also analyzed the relevant transcriptional factors of those DEGs using textmining-based TRRUST database (Han et al., 2015). To help illustrate protein-protein interactions within specific enriched biological processes, the STRING databases (Szklarczyk et al., 2019) were used to draw interactive networks of those key biological pathways using CytoScape (Shannon et al., 2003).

Gene expression by qPCR

The expression of some genes was corroborated by synthesizing cDNA with the High-Capacity RNA-to-cDNA kit (Applied Biosystems). For the qPCR reaction mix, PrimeTime probe-based qPCR assays and PrimeTime Gene Expression Master mix (cat. no. 1055771) were obtained from IDT (Integrated DNA Technologies, Inc). qPCR reactions were run using the Fast mode on a QuantStudio 3 Real-Time PCR Instrument (A28131; Applied Biosystems by Thermo Fisher Scientific). Data were normalized against actin (*Actb*), and the $2^{-\Delta\Delta C_t}$ method was used to calculate relative gene expression value (relative quantity). Relative expression of *Ch25h* (IDT, assay reference Mm.PT.58.42792394.g), *Clec7a* (IDT Mm.PT.58.42049707) *Ilib* (IDT, assay reference Mm.PT.58.42940223), *Tnf* (IDT, assay reference Mm.PT.58.29509614), *Cxcl10* (IDT, assay reference Mm.PT.58.43575827), *Ilio* (IDT, assay reference Mm.PT.58.23604055), and *Actb* (IDT, assay reference Mm.PT.58.33540333) was assessed by qPCR.

Stereotactic intracerebral injections of AD-tau human aggregates in tau transgenic mice

AD-tau was isolated from a human AD brain at a final concentration of 5 $\mu\text{g}/\mu\text{l}$ tau as previously described (Guo et al., 2016; Boluda et al., 2015). AD-tau preparation was diluted to 0.4 $\mu\text{g}/\mu\text{l}$ final concentration and sonicated for 30 s. 2-mo-old T and TCKO mice were anesthetized with isoflurane and placed in a

stereotaxic instrument. Mice were injected in the left hemisphere with 2.5 μl of diluted tau (0.4 $\mu\text{g}/\mu\text{l}$) aggregates per injection site (1 μg of tau, infusion rate 0.2 $\mu\text{g}/\mu\text{l}$) in the DG (bregma: -2.5 mm; lateral: -2.0 mm; depth: -2.0 mm) and cortex (bregma: -2.5 mm; lateral: -2.0 mm; depth: -1.0 mm). Mice were monitored for 7 days after surgery and were sacrificed 45 days after the surgery.

Quantification of oxysterols

Cortex from 6- and 9.5-mo-old mice were homogenized in water (9.9 mg tissue/ml) using Omni Bead Ruptor 24 (Omni International, Inc.). Oxysterols were extracted (liquid-liquid extraction) from 250 μl of homogenate after the addition of 4 ng of the internal standards 24-HC-d7, 25-HC-d6, and 27-HC-d5. Samples were derivatized with nicotinic acid to increase the mass spectrometric sensitivities of the oxysterols and internal standards. Quality control samples were prepared by pooling a portion of study samples and injecting every five samples to monitor instrument performance. The sample analysis was performed with a Shimadzu 20AD HPLC system coupled to a 4000QTRAP mass spectrometer operated in positive multiple reaction monitoring mode. Data processing was conducted with Analyst 1.6.3. The quantification data were reported as pg/mg of tissue.

Lipidomics

Lipidomic analysis was carried out at the Functional Lipidomics Core at Barshop Institute for Longevity and Aging Studies of the University of Texas Health Science Center, San Antonio, TX, USA. Briefly, lipid extracts of cortex from four to five animals per group were prepared and processed as previously described for the quantification of free fatty acids, free cholesterol, and desmosterol (Cashikar et al., 2023). Data processing based on the principles of shotgun lipidomics such as selective ionization, low concentration of lipid solution, and correction for differential isotopologue patterns and kinetics of fragmentation was conducted as previously described (Wang et al., 2017).

Nuclei isolation from frozen hippocampus and snRNA-seq

Frozen hippocampus from five mice per group were pooled in one sample. Nuclei isolation was conducted as described previously (Wang et al., 2021). The 10X Genomics protocol was followed, subjecting the nuclei to a droplet-based 3' end massively parallel snRNA-seq using Chromium Single Cell 3' Reagent Kits (10X Genomics). The libraries were sequenced using an Illumina HiSeq3000 (Illumina). Sample demultiplexing, barcode processing, and single-cell 3' counting were performed using the Cell Ranger Single-Cell Software Suite (10X Genomics). The Seurat v3, MAST, and SoupX R packages were used for subsequent analysis (Butler et al., 2018; Finak et al., 2015; Young and Behjati, 2020). Contamination of cell-free RNA for each sample group was removed using SoupX. Nuclei with mitochondria content >5% or total UMI < 300 or > 6,000 were then removed in Seurat. For each group, the percentage of mitochondria was regressed out, gene counts were normalized, and variable features were identified using the SCTransform function in Seurat. The top 3,000 variable genes were used to integrate experimental groups using the PrepSCTIntegration, FindIntegrationAnchors,

and IntegrateData commands in Seurat. Principal component analysis was performed on the integrated dataset and the first 30 principal components (PCs) were selected for downstream analysis using FindNeighbors and RunUMAP. Clusters were identified using the FindClusters function with a granularity ranging from 0.1 to 1.2. Differential gene expression was performed using LogNormalized RNA counts using MAST. Clusters containing high mitochondrial-genome content or marker genes for more than one coarse cell type (i.e., microglia and excitatory neurons) were removed and data were reclustered using the first 15 PCs and a resolution of 0.2. For microglia subclustering, the microglial cluster was split by the experimental group and re-normalized and integrated as described above. The first 15 PCs were used for the FindNeighbors and RunUMAP functions and clustering resolution was set at 0.3. Differential gene expression was obtained from LogNormalized RNA counts using MAST. Clusters containing high levels of marker gene expression for non-immune cell types were removed and data were reclustered.

Mouse primary microglia treated with tau fibrils

Mixed glia cultures were obtained from cortices of neonatal WT and CKO mice (2–3 days old) as previously described and maintained in cell culture media (DMEM + 10% heat-inactivated FBS + 1× Glutamax + 1× sodium pyruvate and 1× penicillin/streptomycin, all from GIBCO) for 7 days (Cashikar et al., 2023). When large numbers of microglia were observed floating, the flasks were shaken at 200 rpm for 1 h at 37°C. The floating cells were collected by centrifugation and resuspended in cell culture media. Microglia were seeded at a density of 200,000 cells/ml in 12-well plates for gene expression analysis and in 8-well chambers for assessing phagocytosis of tau fibrils. The next day, media was replaced with serum-free media (DMEM/F12 + 1× Glutamax + 1× sodium pyruvate + 0.1% of fatty acid-free BSA and 1× penicillin/streptomycin + 1× insulin, transferrin, and selenite supplement [AR013; R&D Systems] + 25 ng/ml M-CSF [1320-09-10; GoldBio]). Two independent experiments were conducted for tau uptake assay and microglia gene expression.

For tau uptake assay, WT and CKO mouse primary microglia were treated either with ATTO 488-conjugated human recombinant tau-441 (2N4R) P301S mutant protein (0.5 μm) preformed fibrils (cat. no. SPR-329-A488; StressMarq Biosciences) or PBS in serum-free media. After 2 h, cells were rinsed in sterile PBS and fixed in 4% PFA for 12 min. Microglia were rinsed three times in PBS and blocked-permeabilized in 5% goat serum in TBSX. The primary antibody, anti-rat CD68 (rat monoclonal, 1:400; MCA1957; Bio-Rad), was incubated for 2 h at 37°C and removed by rinsing the cells three times with TBS. Cells were incubated with goat anti-rat Alexa 555 and DAPI. Images were acquired with the LSM 880 confocal microscope at 40× (with 2× zoom). Immunoreactivity and number of nuclei were quantified in Fiji.

For assessing gene expression, microglia were treated either with endotoxin-free preformed fibrils of human recombinant tau-441 (2N4R) P301S mutant protein (0.5 μm) expressed with a Baculovirus/sf9 system (cat. no. SPR-471; StressMarq Biosciences) or PBS in serum-free media. After 24 h, RNA was isolated from cells using the Quick-RNA Miniprep Plus Kit

(Zymo Research) and cDNA was synthesized as mentioned before.

Statistics

Data are presented as mean ± SD. GraphPad Prism 9.2 was used to perform statistical analyses. Gaussian distribution was evaluated using the D'Agostino & Pearson normality test. Differences between groups were evaluated by one-way ANOVA tests with post hoc Tukey (parametric) or Kruskal-Wallis (non-parametric) multiple comparisons tests.

Study approval

All animal procedures and experiments were performed under guidelines approved by the animal studies committee at Washington University School of Medicine.

Online supplemental material

Fig. S1 shows supporting evidence for Fig. 1. Fig. S2 shows supporting evidence for Fig. 2. Fig. S3 shows supporting evidence for Fig. 5. Fig. S4 shows supporting evidence for Figs. 6 and 7. Fig. S5 shows the quantitation of desmosterol, cholesterol, and other lipids. Table S1 shows demographic information of the human brain tissue samples. Table S2 shows the total number of DEGs. Table S3 lists DEGs. Table S4 lists DEGs showing only the significant DEGs for each comparison (P value <0.05 and FC of 1.5). Table S5 shows GO term analysis for up- and downregulated genes in T versus WT and TCKO versus T comparisons. Table S6 shows the determination of lipid species in the cortex of WT, T, and TCKO mice by LC/MS. Table S7 shows the summary of the data size of snRNA-seq results. Table S8 shows the integrated average gene expression of cell type-specific markers. Table S9 shows differential gene expression in the microglia cluster. Table S10 shows the relative frequency of the microglia cluster.

Data availability

All sequencing data are available from the Gene Expression Omnibus under accession code GSE250277 (bulk RNA-seq) and GSE242896 (snRNA-seq). All other data are available in the main text or the supplementary material.

Acknowledgments

We also acknowledge technical and equipment support from the Hope Center Alafi Neuroimaging Laboratory, the Washington University Center for Cellular Imaging, and the Genome Technology Access Center at Washington University School of Medicine. We thank Drs. Eric Reiman, Thomas Beach, and Geidy Serrano for the human brain tissue (National Institutes of Health [NIH] grant 5P30AG019610). We thank the technical support for the animal breeding to Kaylee Stillwell, Ramya Chandalavala, Sheryl Eveland, Ainsley Tran, Joseph Reznikov, and Rachel Schave. The authors also wish to acknowledge technical advice from members of the Holtzman, Paul, and Cashikar Labs.

This research was supported by funding from a grant from the National Institute on Aging of the National Institutes of Health under award number U19AG069701 (Project 2: A.G.

Cashikar and D.M. Holtzman) and R01AG081419 (A.G. Cashikar). J.M. Long was supported by career development awards from the National Institute on Aging (K08AG068611) and Alzheimer's Association (AACSF-18-564776). The snRNA-seq experiment was partly supported by the Hope Center for Neurological Disorders and the Washington University Institute of Clinical and Translational Sciences, which is, in part, supported by the National Institutes of Health/National Center for Advancing Translational Sciences (NCATS), Clinical and Translational Science Awards grant #UL1TR002345.

Author contributions: D. Toral-Rios, J.M. Long, D.M. Holtzman, A.G. Cashikar, and S.M. Paul conceived and designed research studies; D. Toral-Rios, J.M. Long, M.R. Strickland, X. Han, and A.G. Cashikar conducted experiments and acquired data; D. Toral-Rios, J.M. Long, J. Yu, J.D. Ulrich, X. Han, and A.G. Cashikar analyzed data; D. Toral-Rios, A.G. Cashikar, and S.M. Paul wrote the manuscript. All authors discussed the results and commented on the manuscript.

Disclosures: J.M. Long reported receiving honoraria from consulting activities with Guidepoint Global, Techspert, and GLG. D.M. Holtzman reported grants from NIH during the conduct of the study; and personal fees from C2N Diagnostics, Genentech, Denali, Cajal Neurosciences, and Asteroid Therapeutics outside the submitted work. S.M. Paul is a shareholder and receives fees or owns equity in Sage Therapeutics, Voyager Therapeutics, Karuna Therapeutics, Rapport Therapeutics, and Eli Lilly and Company outside the submitted work. No other disclosures were reported.

Submitted: 1 November 2023

Revised: 3 January 2024

Accepted: 1 February 2024

References

Akyol, S., Z. Ugur, A. Yilmaz, I. Ustun, S.K.K. Gorti, K. Oh, B. McGuinness, P. Passmore, P.G. Kehoe, M.E. Maddens, et al. 2021. Lipid profiling of Alzheimer's disease brain highlights enrichment in glycerol(phospho) lipid, and sphingolipid metabolism. *Cells*. 10:2591. <https://doi.org/10.3390/cells10102591>

Alessenko, A.V., and E. Albi. 2020. Exploring sphingolipid implications in neurodegeneration. *Front. Neurol.* 11:437. <https://doi.org/10.3389/fneur.2020.00437>

Alonso, A., T. Zaidi, M. Novak, I. Grundke-Iqbal, and K. Iqbal. 2001. Hyperphosphorylation induces self-assembly of tau into tangles of paired helical filaments/straight filaments. *Proc. Natl. Acad. Sci. USA*. 98: 6923–6928. <https://doi.org/10.1073/pnas.121119298>

Bauman, D.R., A.D. Bitmansour, J.G. McDonald, B.M. Thompson, G. Liang, and D.W. Russell. 2009. 25-Hydroxycholesterol secreted by macrophages in response to toll-like receptor activation suppresses immunoglobulin A production. *Proc. Natl. Acad. Sci. USA*. 106:16764–16769. <https://doi.org/10.1073/pnas.0909142106>

Boluda, S., M. Iba, B. Zhang, K.M. Raible, V.M. Lee, and J.Q. Trojanowski. 2015. Differential induction and spread of tau pathology in young PS19 tau transgenic mice following intracerebral injections of pathological tau from Alzheimer's disease or corticobasal degeneration brains. *Acta Neuropathol.* 129:221–237. <https://doi.org/10.1007/s00401-014-1373-0>

Butler, A., P. Hoffman, P. Smibert, E. Papalexis, and R. Satija. 2018. Integrating single-cell transcriptomic data across different conditions, technologies, and species. *Nat. Biotechnol.* 36:411–420. <https://doi.org/10.1038/nbt.4096>

Butler, C.A., A.S. Popescu, E.J.A. Kitchener, D.H. Allendorf, M. Puigdemívol, and G.C. Brown. 2021. Microglial phagocytosis of neurons in

neurodegeneration, and its regulation. *J. Neurochem.* 158:621–639. <https://doi.org/10.1111/jnc.15327>

Cashikar, A.G., D. Toral-Rios, D. Timm, J. Romero, M. Strickland, J.M. Long, X. Han, D.M. Holtzman, and S.M. Paul. 2023. Regulation of astrocyte lipid metabolism and ApoE secretion by the microglial oxysterol, 25-hydroxycholesterol. *J. Lipid Res.* 64:100350. <https://doi.org/10.1016/j.jlr.2023.100350>

Chen, X., M. Firulyova, M. Manis, J. Herz, I. Smirnov, E. Aladyeva, C. Wang, X. Bao, M.B. Finn, H. Hu, et al. 2023. Microglia-mediated T cell infiltration drives neurodegeneration in tauopathy. *Nature*. 615:668–677. <https://doi.org/10.1038/s41586-023-05788-0>

Chen, Y., and M. Colonna. 2021. Microglia in Alzheimer's disease at single-cell level. Are there common patterns in humans and mice? *J. Exp. Med.* 218: e20202717. <https://doi.org/10.1084/jem.20202717>

Chew, H., V.A. Solomon, and A.N. Fonteh. 2020. Involvement of lipids in Alzheimer's disease pathology and potential therapies. *Front. Physiol.* 11: 598. <https://doi.org/10.3389/fphys.2020.00598>

Colonna, M., and O. Butovsky. 2017. Microglia function in the central nervous system during health and neurodegeneration. *Annu. Rev. Immunol.* 35: 441–468. <https://doi.org/10.1146/annurev-immunol-051116-052358>

Cutler, R.G., J. Kelly, K. Storie, W.A. Pedersen, E. Tammara, K. Hatanpaa, J.C. Troncoso, and M.P. Mattson. 2004. Involvement of oxidative stress-induced abnormalities in ceramide and cholesterol metabolism in brain aging and Alzheimer's disease. *Proc. Natl. Acad. Sci. USA*. 101: 2070–2075. <https://doi.org/10.1073/pnas.0305799101>

Cyster, J.G., E.V. Dang, A. Reboldi, and T. Yi. 2014. 25-Hydroxycholesterols in innate and adaptive immunity. *Nat. Rev. Immunol.* 14:731–743. <https://doi.org/10.1038/nri3755>

Dang, E.V., J.G. McDonald, D.W. Russell, and J.G. Cyster. 2017. Oxysterol restraint of cholesterol synthesis prevents Aim2 inflammasome activation. *Cell*. 171:1057–1071.e11. <https://doi.org/10.1016/j.cell.2017.09.029>

Deczkowska, A., H. Keren-Shaul, A. Weiner, M. Colonna, M. Schwartz, and I. Amit. 2018. Disease-associated microglia: A universal immune sensor of neurodegeneration. *Cell*. 173:1073–1081. <https://doi.org/10.1016/j.cell.2018.05.003>

Dejanovic, B., M.A. Huntley, A. De Maziere, W.J. Meilandt, T. Wu, K. Srinivasan, Z. Jiang, V. Gandham, B.A. Friedman, H. Ngu, et al. 2018. Changes in the synaptic proteome in tauopathy and rescue of tau-induced synapse loss by C1q antibodies. *Neuron*. 100:1322–1336.e7. <https://doi.org/10.1016/j.neuron.2018.10.014>

DeVos, S.L., B.T. Corjuc, D.H. Oakley, C.K. Nobuhara, R.N. Bannon, A. Chase, C. Commins, J.A. Gonzalez, P.M. Dooley, M.P. Frosch, and B.T. Hyman. 2018. Synaptic tau seeding precedes tau pathology in human Alzheimer's disease brain. *Front. Neurosci.* 12:267. <https://doi.org/10.3389/fnins.2018.00267>

Di Paolo, G., and T.W. Kim. 2011. Linking lipids to Alzheimer's disease: Cholesterol and beyond. *Nat. Rev. Neurosci.* 12:284–296. <https://doi.org/10.1038/nrn3012>

Dobin, A., C.A. Davis, F. Schlesinger, J. Drenkow, C. Zaleski, S. Jha, P. Batut, M. Chaisson, and T.R. Gingeras. 2013. STAR: Ultrafast universal RNA-seq aligner. *Bioinformatics*. 29:15–21. <https://doi.org/10.1093/bioinformatics/bts635>

Falabella, M., H.J. Vernon, M.G. Hanna, S.M. Claypool, and R.D.S. Pitceathly. 2021. Cardiolipin, mitochondria, and neurological disease. *Trends Endocrinol. Metab.* 32:224–237. <https://doi.org/10.1016/j.tem.2021.01.006>

Feringa, F.M., and R. van der Kant. 2021. Cholesterol and Alzheimer's disease; from risk genes to pathological effects. *Front. Aging Neurosci.* 13:690372. <https://doi.org/10.3389/fnagi.2021.690372>

Ferris, H.A., R.J. Perry, G.V. Moreira, G.I. Shulman, J.D. Horton, and C.R. Kahn. 2017. Loss of astrocyte cholesterol synthesis disrupts neuronal function and alters whole-body metabolism. *Proc. Natl. Acad. Sci. USA*. 114:1189–1194. <https://doi.org/10.1073/pnas.1620506114>

Finak, G., A. McDavid, M. Yajima, J. Deng, V. Gersuk, A.K. Shalek, C.K. Slichter, H.W. Miller, M.J. McElrath, M. Prlic, et al. 2015. MAST: A flexible statistical framework for assessing transcriptional changes and characterizing heterogeneity in single-cell RNA sequencing data. *Genome Biol.* 16:278. <https://doi.org/10.1186/s13059-015-0844-5>

Friedman, B.A., K. Srinivasan, G. Ayalon, W.J. Meilandt, H. Lin, M.A. Huntley, Y. Cao, S.H. Lee, P.C.G. Haddick, H. Ngu, et al. 2018. Diverse brain myeloid expression profiles reveal distinct microglial activation states and aspects of Alzheimer's disease not evident in mouse models. *Cell Rep.* 22:832–847. <https://doi.org/10.1016/j.celrep.2017.12.066>

Fu, H., F. Spieler, J. Großmann, D. Riemann, M. Larisch, B. Hiebl, K. Schlecht, C. Jaschke, B. Bartling, B. Hofmann, et al. 2014. Interleukin-1 potently contributes to 25-hydroxycholesterol-induced synergistic cytokine

- production in smooth muscle cell-monocyte interactions. *Atherosclerosis*. 237:443–452. <https://doi.org/10.1016/j.atherosclerosis.2014.10.002>
- Gate, D., N. Saligrama, O. Leventhal, A.C. Yang, M.S. Unger, J. Middeldorp, K. Chen, B. Lehallier, D. Channappa, M.B. De Los Santos, et al. 2020. Clonally expanded CD8 T cells patrol the cerebrospinal fluid in Alzheimer's disease. *Nature*. 577:399–404. <https://doi.org/10.1038/s41586-019-1895-7>
- Giannakopoulos, P., F.R. Herrmann, T. Bussi re, C. Bouras, E. Kovari, D.P. Perl, J.H. Morrison, G. Gold, and P.R. Hof. 2003. Tangle and neuron numbers, but not amyloid load, predict cognitive status in Alzheimer's disease. *Neurology*. 60:1495–1500. <https://doi.org/10.1212/01.WNL.0000063311.58879.01>
- Gold, E.S., A.H. Diercks, I. Podolsky, R.L. Podyminogin, P.S. Askovich, P.M. Treuting, and A. Aderem. 2014. 25-Hydroxycholesterol acts as an amplifier of inflammatory signaling. *Proc. Natl. Acad. Sci. USA*. 111:10666–10671. <https://doi.org/10.1073/pnas.1404271111>
- Gratuze, M., C.E. Leyns, A.D. Sauerbeck, M.K. St-Pierre, M. Xiong, N. Kim, J.R. Serrano, M.E. Tremblay, T.T. Kummer, M. Colonna, et al. 2020. Impact of TREM2R47H variant on tau pathology-induced gliosis and neurodegeneration. *J. Clin. Invest.* 130:4954–4968. <https://doi.org/10.1172/JCI138179>
- Greten, F.R., M.C. Arkan, J. Bollrath, L.C. Hsu, J. Goode, C. Miething, S.I. Goktuna, M. Neuenhahn, J. Fierer, S. Paxian, et al. 2007. NF-kappaB is a negative regulator of IL-1beta secretion as revealed by genetic and pharmacological inhibition of IKKbeta. *Cell*. 130:918–931. <https://doi.org/10.1016/j.cell.2007.07.009>
- Griffiths, W.J., and Y. Wang. 2022. Cholesterol metabolism: From lipidomics to immunology. *J. Lipid Res.* 63:100165. <https://doi.org/10.1016/j.jlr.2021.100165>
- Guo, J.L., S. Narasimhan, L. Changolkar, Z. He, A. Stieber, B. Zhang, R.J. Gathagan, M. Iba, J.D. McBride, J.Q. Trojanowski, and V.M. Lee. 2016. Unique pathological tau conformers from Alzheimer's brains transmit tau pathology in nontransgenic mice. *J. Exp. Med.* 213:2635–2654. <https://doi.org/10.1084/jem.20160833>
- Han, H., H. Shim, D. Shin, J.E. Shim, Y. Ko, J. Shin, H. Kim, A. Cho, E. Kim, T. Lee, et al. 2015. TRRUST: A reference database of human transcriptional regulatory interactions. *Sci. Rep.* 5:11432. <https://doi.org/10.1038/srep11432>
- Hopperton, K.E., D. Mohammad, M.O. Tr panier, V. Giuliano, and R.P. Bazinet. 2018. Markers of microglia in post-mortem brain samples from patients with Alzheimer's disease: A systematic review. *Mol. Psychiatry*. 23:177–198. <https://doi.org/10.1038/mp.2017.246>
- Izumi, Y., A.G. Cashikar, K. Krishnan, S.M. Paul, D.F. Covey, S.J. Mennerick, and C.F. Zorumski. 2021. A proinflammatory stimulus disrupts hippocampal plasticity and learning via microglial activation and 25-hydroxycholesterol. *J. Neurosci.* 41:10054–10064. <https://doi.org/10.1523/JNEUROSCI.1502-21.2021>
- Jang, J., S. Park, H. Jin Hur, H.J. Cho, I. Hwang, Y. Pyo Kang, I. Im, H. Lee, E. Lee, W. Yang, et al. 2016. 25-hydroxycholesterol contributes to cerebral inflammation of X-linked adrenoleukodystrophy through activation of the NLRP3 inflammasome. *Nat. Commun.* 7:13129. <https://doi.org/10.1038/ncomms13129>
- Jiang, S., N.M. Maphis, J. Binder, D. Chisholm, L. Weston, W. Duran, C. Peterson, A. Zimmerman, M.A. Mandell, S.D. Jett, et al. 2021. Proteopathic tau primes and activates interleukin-1  via myeloid-cell-specific MyD88- and NLRP3-ASC-inflammasome pathway. *Cell Rep.* 36:109720. <https://doi.org/10.1016/j.celrep.2021.109720>
- Jicha, G.A., R. Bowser, I.G. Kazam, and P. Davies. 1997. Alz-50 and MC-1, a new monoclonal antibody raised to paired helical filaments, recognize conformational epitopes on recombinant tau. *J. Neurosci. Res.* 48:128–132. [https://doi.org/10.1002/\(SICI\)1097-4547\(19970415\)48:2<128::AID-JNRS>3.0.CO;2-E](https://doi.org/10.1002/(SICI)1097-4547(19970415)48:2<128::AID-JNRS>3.0.CO;2-E)
- Jorfi, M., J. Park, C.K. Hall, C.J. Lin, M. Chen, D. Von Maydell, J.M. Kruskop, B. Kang, Y. Choi, D. Prokopenko, et al. 2023. Infiltrating Cd8(+) T cells exacerbate Alzheimer's disease pathology in A 3d human neuroimmune axis model. *Nat Neurosci.* 26:1489–1504. <https://doi.org/10.1038/s41593-023-01415-3>
- Karch, C.M., and A.M. Goate. 2015. Alzheimer's disease risk genes and mechanisms of disease pathogenesis. *Biol. Psychiatry*. 77:43–51. <https://doi.org/10.1016/j.biopsych.2014.05.006>
- Keren-Shaul, H., A. Spinrad, A. Weiner, O. Matcovitch-Natan, R. Dvir-Szternfeld, T.K. Ulland, E. David, K. Baruch, D. Lara-Astaiso, and B. Toth, et al. 2017. A unique microglia type associated with restricting development of Alzheimer's disease. *Cell*. 169:1276–1290.e17. <https://doi.org/10.1016/j.cell.2017.05.018>
- Kim, J., S. Selvaraji, S.W. Kang, W.T. Lee, C.L. Chen, H. Choi, E.H. Koo, D.G. Jo, K. Leong Lim, Y.A. Lim, and T.V. Arumugam. 2019. Cerebral transcriptome analysis reveals age-dependent progression of neuroinflammation in P301S mutant tau transgenic male mice. *Brain Behav. Immun.* 80:344–357. <https://doi.org/10.1016/j.bbi.2019.04.011>
- Krasemann, S., C. Madore, R. Cialic, C. Baufeld, N. Calcagno, R. El Fatimy, L. Beckers, E. O'loughlin, Y. Xu, Z. Fanek, et al. 2017. The Trem2-ApoE pathway drives the transcriptional phenotype of dysfunctional microglia in neurodegenerative diseases. *Immunity*. 47:566–581.e9. <https://doi.org/10.1016/j.immuni.2017.08.008>
- Laurent, C., G. Doroth e, S. Hunot, E. Martin, Y. Monnet, M. Duchamp, Y. Dong, F.P. L geron, A. Leboucher, S. Burnouf, et al. 2017. Hippocampal T cell infiltration promotes neuroinflammation and cognitive decline in a mouse model of tauopathy. *Brain*. 140:184–200. <https://doi.org/10.1093/brain/aww270>
- Leyns, C.E.G., and D.M. Holtzman. 2017. Glial contributions to neurodegeneration in tauopathies. *Mol. Neurodegener.* 12:50. <https://doi.org/10.1186/s13024-017-0192-x>
- Leyns, C.E.G., J.D. Ulrich, M.B. Finn, F.R. Stewart, L.J. Koscal, J. Remolina Serrano, G.O. Robinson, E. Anderson, M. Colonna, and D.M. Holtzman. 2017. TREM2 deficiency attenuates neuroinflammation and protects against neurodegeneration in a mouse model of tauopathy. *Proc. Natl. Acad. Sci. USA*. 114:11524–11529. <https://doi.org/10.1073/pnas.1710311114>
- Liao, Y., G.K. Smyth, and W. Shi. 2014. featureCounts: An efficient general purpose program for assigning sequence reads to genomic features. *Bioinformatics*. 30:923–930. <https://doi.org/10.1093/bioinformatics/btt656>
- Litvinchuk, A., Y.W. Wan, D.B. Swartzlander, F. Chen, A. Cole, N.E. Propson, Q. Wang, B. Zhang, Z. Liu, and H. Zheng. 2018. Complement C3ar activation attenuates tau pathology and reverses an immune network deregulated in tauopathy models and Alzheimer's disease. *Neuron*. 100:1337–1353.e5. <https://doi.org/10.1016/j.neuron.2018.10.031>
- Liu, C., X.V. Yang, J. Wu, C. Kuei, N.S. Mani, L. Zhang, J. Yu, S.W. Sutton, N. Qin, H. Banie, et al. 2011. Oxysterols direct B-cell migration through EB12. *Nature*. 475:519–523. <https://doi.org/10.1038/nature10226>
- Liu, R., A.Z. Holik, S. Su, N. Jansz, K. Chen, H.S. Leong, M.E. Blewitt, M.L. Asselin-Labat, G.K. Smyth, and M.E. Ritchie. 2015. Why weight? Modelling sample and observational level variability improves power in RNA-seq analyses. *Nucleic Acids Res.* 43:e97. <https://doi.org/10.1093/nar/gkv412>
- Liu, S.Y., R. Aliyari, K. Chikere, G. Li, M.D. Marsden, J.K. Smith, O. Pernet, H. Guo, R. Nusbaum, J.A. Zack, et al. 2013. Interferon-inducible cholesterol-25-hydroxylase broadly inhibits viral entry by production of 25-hydroxycholesterol. *Immunity*. 38:92–105. <https://doi.org/10.1016/j.immuni.2012.11.005>
- Long, J.M., and D.M. Holtzman. 2019. Alzheimer disease: An update on pathobiology and treatment strategies. *Cell*. 179:312–339. <https://doi.org/10.1016/j.cell.2019.09.001>
- Lund, E.G., T.A. Kerr, J. Sakai, W.P. Li, and D.W. Russell. 1998. cDNA cloning of mouse and human cholesterol 25-hydroxylases, polytopic membrane proteins that synthesize a potent oxysterol regulator of lipid metabolism. *J. Biol. Chem.* 273:34316–34327. <https://doi.org/10.1074/jbc.273.51.34316>
- Monteiro-Cardoso, V.F., M.M. Oliveira, T. Melo, M.R. Domingues, P.I. Moreira, E. Ferreira, F. Peixoto, and R.A. Videira. 2015. Cardiolipin profile changes are associated to the early synaptic mitochondrial dysfunction in Alzheimer's disease. *J. Alzheimers Dis.* 43:1375–1392. <https://doi.org/10.3233/JAD-141002>
- Poliani, P.L., Y. Wang, E. Fontana, M.L. Robinette, Y. Yamanishi, S. Gilfillan, and M. Colonna. 2015. TREM2 sustains microglial expansion during aging and response to demyelination. *J. Clin. Invest.* 125:2161–2170. <https://doi.org/10.1172/JCI77983>
- Radhakrishnan, A., Y. Ikeda, H.J. Kwon, M.S. Brown, and J.L. Goldstein. 2007. Sterol-regulated transport of SREBPs from endoplasmic reticulum to Golgi: Oxysterols block transport by binding to insig. *Proc. Natl. Acad. Sci. USA*. 104:6511–6518. <https://doi.org/10.1073/pnas.0700899104>
- Reboldi, A., E.V. Dang, J.G. McDonald, G. Liang, D.W. Russell, and J.G. Cyster. 2014. Inflammation. 25-Hydroxycholesterol suppresses interleukin-1-driven inflammation downstream of type I interferon. *Science*. 345:679–684. <https://doi.org/10.1126/science.1254790>
- Ritchie, M.E., B. Phipson, D. Wu, Y. Hu, C.W. Law, W. Shi, and G.K. Smyth. 2015. Limma powers differential expression analysis for RNA-seq and microarray studies. *Nucleic Acids Res.* 43:e47. <https://doi.org/10.1093/nar/gkv007>
- Robinson, M.D., D.J. McCarthy, and G.K. Smyth. 2010. edgeR: A bioconductor package for differential expression analysis of digital gene

- expression data. *Bioinformatics*. 26:139–140. <https://doi.org/10.1093/bioinformatics/btp616>
- Sayed, F.A., M. Telpoukhovskaia, L. Kodama, Y. Li, Y. Zhou, D. Le, A. Hauduc, C. Ludwig, F. Gao, C. Clelland, et al. 2018. Differential effects of partial and complete loss of TREM2 on microglial injury response and tauopathy. *Proc. Natl. Acad. Sci. USA*. 115:10172–10177. <https://doi.org/10.1073/pnas.1811411115>
- Schwabenland, M., W. Brück, J. Priller, C. Stadelmann, H. Lassmann, and M. Prinz. 2021. Analyzing microglial phenotypes across neuropathologies: A practical guide. *Acta Neuropathol.* 142:923–936. <https://doi.org/10.1007/s00401-021-02370-8>
- Seo, D.O., D. O'Donnell, N. Jain, J.D. Ulrich, J. Herz, Y. Li, M. Lemieux, J. Cheng, H. Hu, J.R. Serrano, et al. 2023. ApoE isoform- and microbiota-dependent progression of neurodegeneration in a mouse model of tauopathy. *Science*. 379:eadd1236. <https://doi.org/10.1126/science.add1236>
- Shannon, P., A. Markiel, O. Ozier, N.S. Baliga, J.T. Wang, D. Ramage, N. Amin, B. Schwikowski, and T. Ideker. 2003. Cytoscape: A software environment for integrated models of biomolecular interaction networks. *Genome Res.* 13:2498–2504. <https://doi.org/10.1101/gr.1239303>
- Shi, Y., M. Manis, J. Long, K. Wang, P.M. Sullivan, J. Remolina Serrano, R. Hoyle, and D.M. Holtzman. 2019. Microglia drive APOE-dependent neurodegeneration in a tauopathy mouse model. *J. Exp. Med.* 216: 2546–2561. <https://doi.org/10.1084/jem.20190980>
- Shi, Y., K. Yamada, S.A. Liddel, S.T. Smith, L. Zhao, W. Luo, R.M. Tsai, S. Spina, L.T. Grinberg, J.C. Rojas, et al. 2017. ApoE4 markedly exacerbates tau-mediated neurodegeneration in a mouse model of tauopathy. *Nature*. 549:523–527. <https://doi.org/10.1038/nature24016>
- Smith, L.L. 1987. Cholesterol autooxidation 1981–1986. *Chem. Phys. Lipids*. 44: 87–125. [https://doi.org/10.1016/0009-3084\(87\)90046-6](https://doi.org/10.1016/0009-3084(87)90046-6)
- Sobue, A., O. Komine, Y. Hara, F. Endo, H. Mizoguchi, S. Watanabe, S. Murayama, T. Saito, T.C. Saido, N. Sahara, et al. 2021. Microglial gene signature reveals loss of homeostatic microglia associated with neurodegeneration of Alzheimer's disease. *Acta Neuropathol. Commun.* 9:1. <https://doi.org/10.1186/s40478-020-01099-x>
- Sun, J.H., J.T. Yu, and L. Tan. 2015. The role of cholesterol metabolism in Alzheimer's disease. *Mol. Neurobiol.* 51:947–965. <https://doi.org/10.1007/s12035-014-8749-y>
- Szklarczyk, D., A.L. Gable, D. Lyon, A. Junge, S. Wyder, J. Huerta-Cepas, M. Simonovic, N.T. Doncheva, J.H. Morris, P. Bork, et al. 2019. STRING v11: Protein-protein association networks with increased coverage, supporting functional discovery in genome-wide experimental datasets. *Nucleic Acids Res.* 47:D607–D613. <https://doi.org/10.1093/nar/gky1131>
- Testa, G., E. Staurengi, C. Zerbinati, S. Gargiulo, L. Iuliano, G. Giaccone, F. Fantò, G. Poli, G. Leonarduzzi, and P. Gamba. 2016. Changes in brain oxysterols at different stages of Alzheimer's disease: Their involvement in neuroinflammation. *Redox Biol.* 10:24–33. <https://doi.org/10.1016/j.redox.2016.09.001>
- Tsumagari, K., Y. Sato, A. Shimozawa, H. Aoyagi, H. Okano, and J. Kuromitsu. 2022. Co-expression network analysis of human tau-transgenic mice reveals protein modules associated with tau-induced pathologies. *iScience*. 25:104832. <https://doi.org/10.1016/j.isci.2022.104832>
- Tuck, B.J., L.V.C. Miller, T. Katsinelos, A.E. Smith, E.L. Wilson, S. Keeling, S. Cheng, M.J. Vaysburd, C. Knox, L. Tredgett, et al. 2022. Cholesterol determines the cytosolic entry and seeded aggregation of tau. *Cell Rep.* 39:110776. <https://doi.org/10.1016/j.celrep.2022.110776>
- Udeochu, J.C., S. Amin, Y. Huang, L. Fan, E.R.S. Torres, G.K. Carling, B. Liu, H. McGurran, G. Coronas-Samano, G. Kauwe, et al. 2023. Tau activation of microglial cGAS-IFN reduces MEF2C-mediated cognitive resilience. *Nat. Neurosci.* 26:737–750. <https://doi.org/10.1038/s41593-023-01315-6>
- Varma, V.R., H. Büşra Lüleci, A.M. Oommen, S. Varma, C.T. Blackshear, M.E. Griswold, Y. An, J.A. Roberts, R. O'Brien, O. Pletnikova, et al. 2021. Abnormal brain cholesterol homeostasis in Alzheimer's disease—a targeted metabolomic and transcriptomic study. *NPJ Aging Mech. Dis.* 7:11. <https://doi.org/10.1038/s41514-021-00064-9>
- Wang, C., L. Fan, R.R. Khawaja, B. Liu, L. Zhan, L. Kodama, M. Chin, Y. Li, D. Le, Y. Zhou, et al. 2022. Microglial NF- κ B drives tau spreading and toxicity in a mouse model of tauopathy. *Nat. Commun.* 13:1969. <https://doi.org/10.1038/s41467-022-29552-6>
- Wang, C., M. Xiong, M. Gratuze, X. Bao, Y. Shi, P.S. Andhey, M. Manis, C. Schroeder, Z. Yin, C. Madore, et al. 2021. Selective removal of astrocytic ApoE4 strongly protects against tau-mediated neurodegeneration and decreases synaptic phagocytosis by microglia. *Neuron*. 109:1657–1674.e7. <https://doi.org/10.1016/j.neuron.2021.03.024>
- Wang, M., C. Wang, and X. Han. 2017. Selection of internal standards for accurate quantification of complex lipid species in biological extracts by electrospray ionization mass spectrometry—What, how and why? *Mass Spectrom. Rev.* 36:693–714. <https://doi.org/10.1002/mas.21492>
- Wanke, F., S. Moos, A.L. Croxford, A.P. Heinen, S. Gräf, B. Kalt, D. Tischner, J. Zhang, I. Christen, J. Bruttger, et al. 2017. EBI2 is highly expressed in multiple sclerosis lesions and promotes early CNS migration of encephalitogenic CD4 T cells. *Cell Rep.* 18:1270–1284. <https://doi.org/10.1016/j.celrep.2017.01.020>
- Wong, M.Y., M. Lewis, J.J. Doherty, Y. Shi, A.G. Cashikar, A. Amelianchik, S. Tymchuk, P.M. Sullivan, M. Qian, D.F. Covey, et al. 2020. 25-Hydroxycholesterol amplifies microglial IL-1 β production in an apoE isoform-dependent manner. *J. Neuroinflammation*. 17:192. <https://doi.org/10.1186/s12974-020-01869-3>
- Wood, P.L. 2012. Lipidomics of Alzheimer's disease: Current status. *Alzheimers Res. Ther.* 4:5. <https://doi.org/10.1186/alzrt103>
- Yoshiyama, Y., M. Higuchi, B. Zhang, S.M. Huang, N. Iwata, T.C. Saido, J. Maeda, T. Suhara, J.Q. Trojanowski, and V.M. Lee. 2007. Synapse loss and microglial activation precede tangles in a P301S tauopathy mouse model. *Neuron*. 53:337–351. <https://doi.org/10.1016/j.neuron.2007.01.010>
- Young, M.D., and S. Behjati. 2020. SoupX removes ambient RNA contamination from droplet-based single-cell RNA sequencing data. *Gigascience*. 9:giaa151. <https://doi.org/10.1093/gigascience/giaa151>
- Zhou, Y., W.M. Song, P.S. Andhey, A. Swain, T. Levy, K.R. Miller, P.L. Poliani, M. Cominelli, S. Grover, S. Gilfillan, et al. 2020. Human and mouse single-nucleus transcriptomics reveal TREM2-dependent and TREM2-independent cellular responses in Alzheimer's disease. *Nat. Med.* 26: 131–142. <https://doi.org/10.1038/s41591-019-0695-9>
- Zhou, Y., B. Zhou, L. Pache, M. Chang, A.H. Khodabakhshi, O. Tanaseichuk, C. Benner, and S.K. Chanda. 2019. Metascape provides a biologist-oriented resource for the analysis of systems-level datasets. *Nat. Commun.* 10: 1523. <https://doi.org/10.1038/s41467-019-09234-6>
- Zhu, Z., Y. Hu, Y. Zhou, Y. Zhang, L. Yu, L. Tao, A. Guo, and Q. Fang. 2019. Macrophage migration inhibitory factor promotes chemotaxis of astrocytes through regulation of cholesterol 25-hydroxylase following rat spinal cord injury. *Neuroscience*. 408:349–360. <https://doi.org/10.1016/j.neuroscience.2019.04.022>
- Zu, S., Y.Q. Deng, C. Zhou, J. Li, L. Li, Q. Chen, X.F. Li, H. Zhao, S. Gold, J. He, et al. 2020. 25-Hydroxycholesterol is a potent SARS-CoV-2 inhibitor. *Cell Res.* 30:1043–1045. <https://doi.org/10.1038/s41422-020-00398-1>

Supplemental material

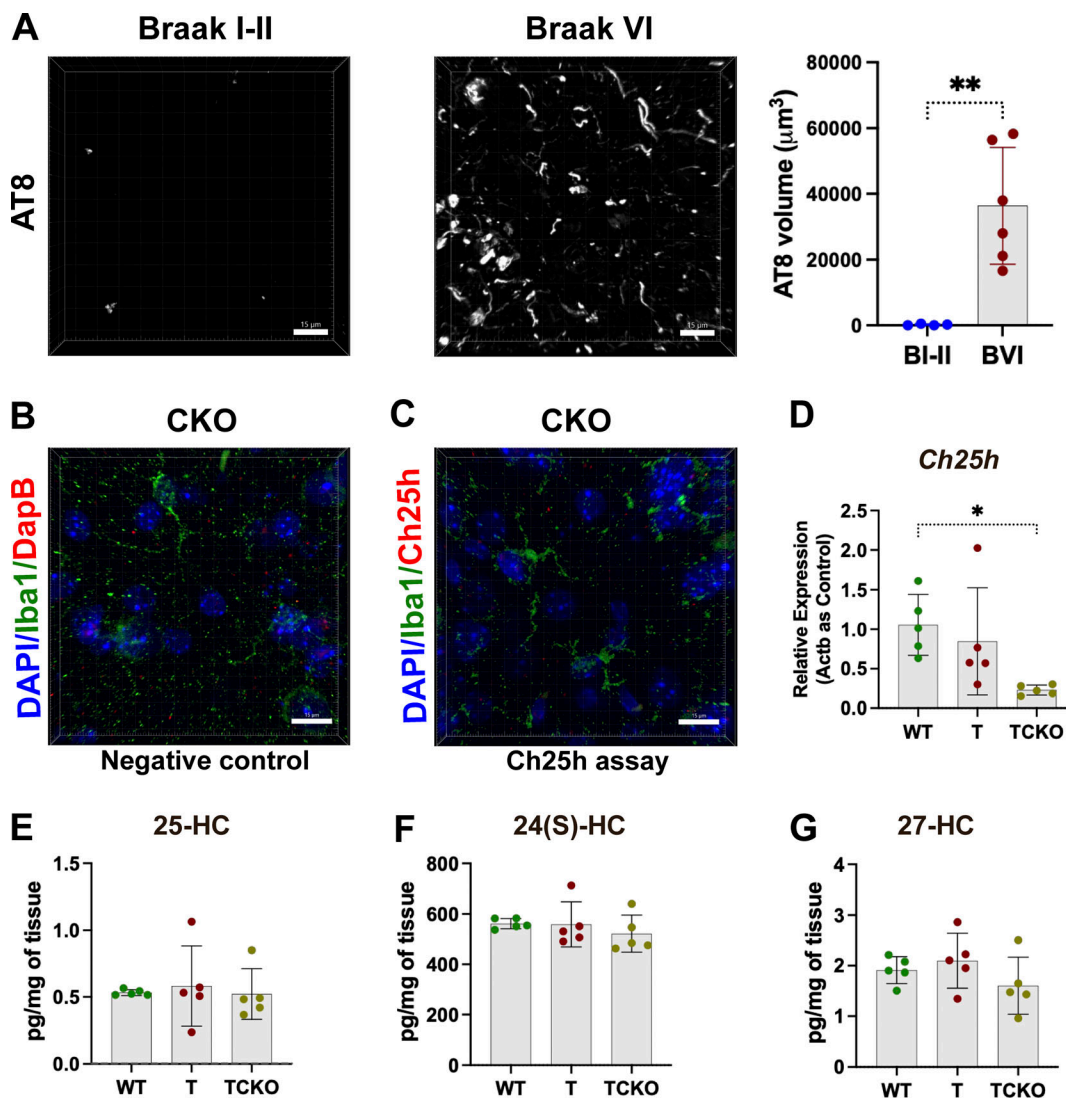


Figure S1. **Ch25h is expressed mainly in microglia in AD and PS19 mice brains.** (A) Representative images of a Braak VI AD frontal cortex section stained with AT8 (p-tau) and quantification of the volumes of AT8 immunoreactivity. (B and C) Representative 3D Imaris images from the hippocampus of 9.5-mo-old female *Ch25h* KO (CKO) mouse stained with DapB (B, negative control) or *Ch25h* assay (C) RNAscope assay, DAPI and Iba1. (D) Relative expression of *Ch25h* in the hippocampus of 6-mo-old WT, T, and TCKO female mice ($n = 5$ for each group). (E-G) Levels of 25-HC (E), 24-hydroxycholesterol (F), and 27-hydroxycholesterol (G) were quantified in the hippocampus of 6-mo-old female WT ($n = 5$), T ($n = 5$), and TCKO ($n = 5$) mice. Scale bar, 15 μm . Data are expressed as mean \pm SD; one-way ANOVA with Tukey's post hoc test (two-sided) was used for all statistical analyses. * $P < 0.05$, ** $P < 0.01$.

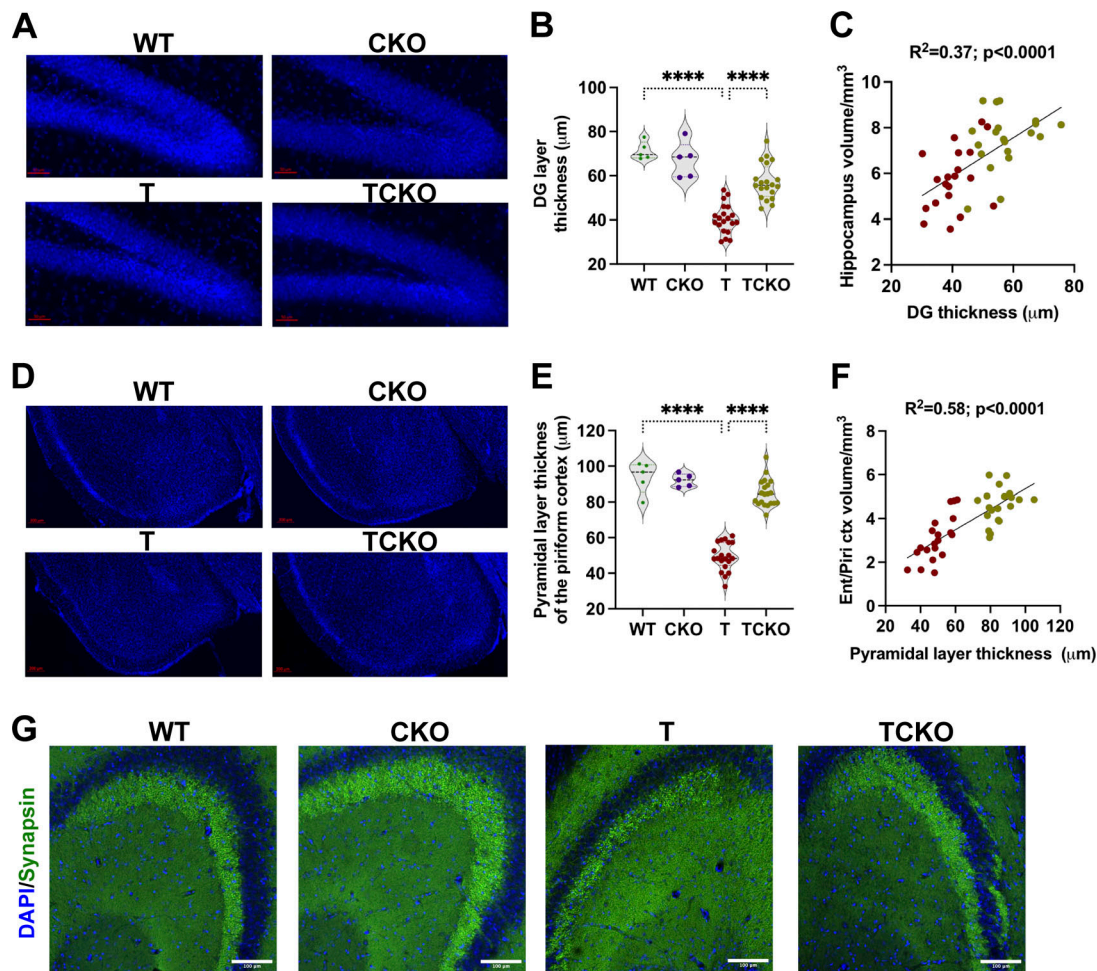


Figure S2. **Ch25h deficiency reduces neuronal loss in PS19 mice.** (A, B, D, and E) Representative images (A and D) and corresponding layer thicknesses (B and E) of 9.5-mo-old WT, Ch25h KO (CKO), PS19 (T), and PS19/Ch25h KO (TCKO) mouse brain sections stained with DAPI (scale bar, 50 μm). The thickness of the granule cell layer in DG (A and B) and the pyramidal layer in the piriform cortex (D and E) are shown. (C, F, and G) Pearson correlation analysis (two-sided) between DG (C) cell layer thickness with the hippocampal volume as well as the correlation between pyramidal layer of the piriform cortex (F) with the volume of entorhinal cortex are shown for tau mice—T (red) and TCKO (asparagus). Representative images (G) corresponding to Fig. 2 H (scale bar, 50 μm , at 20 \times) from mouse brain sections stained with synapsin 1a/lb antibody (green) and DAPI (blue) in the CA3 region of the hippocampus (G). Data are expressed as mean \pm SD; one-way ANOVA with Tukey's post hoc test (two-sided) was used for all statistical analysis. **** $P < 0.0001$. Ent: entorhinal cortex, Piri: piriform cortex.

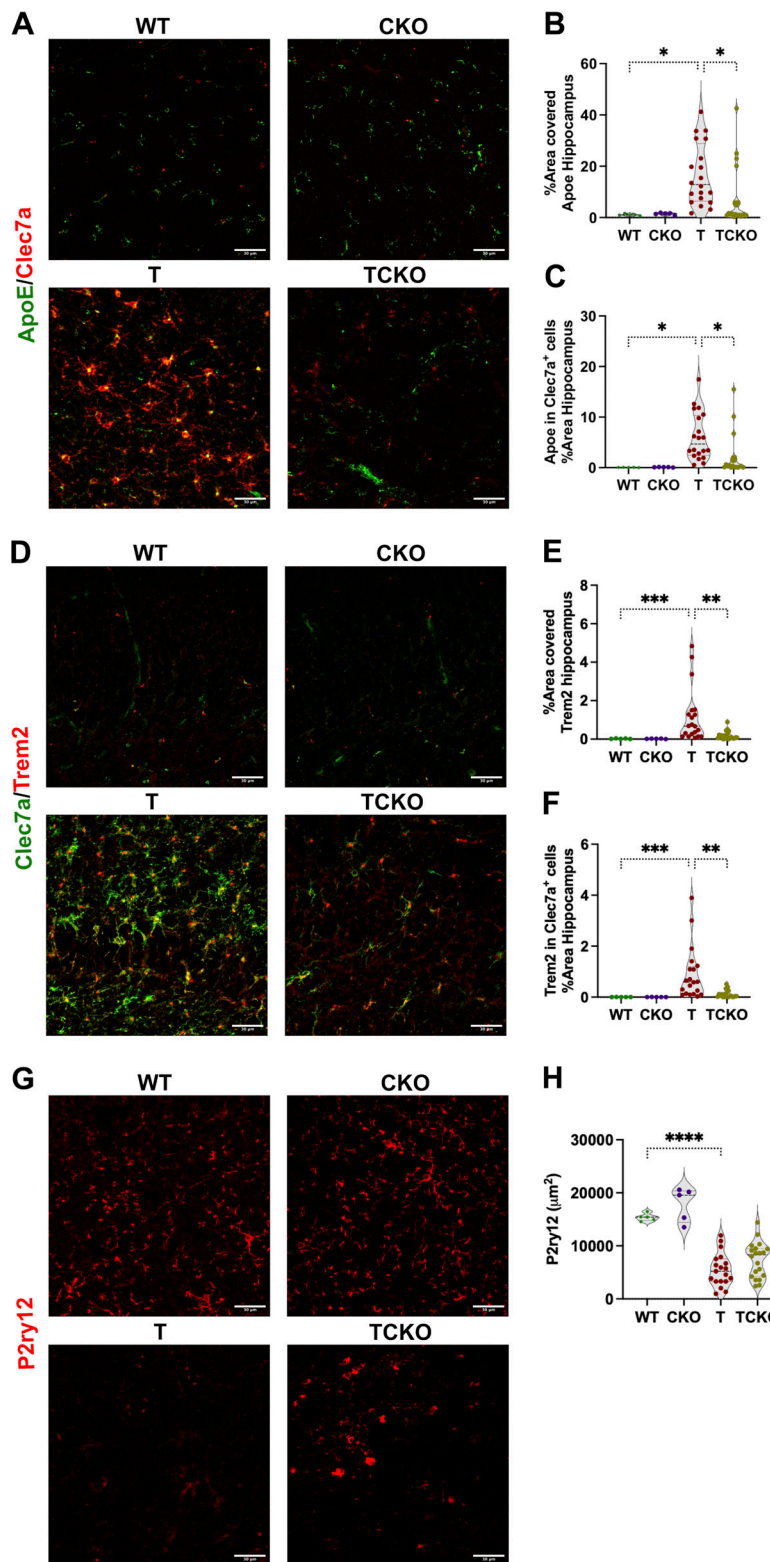


Figure S3. **Ch25h deficiency in PS19 mice decreases DAM markers without altering homeostatic microglia.** (A) Representative images from a double stain of the DAM markers ApoE (green) and Clec7a (red) in 9.5-mo-old WT ($n = 5$), Ch25h KO (CKO; $n = 5$), PS19 (T; $n = 20$), and PS19/Ch25h KO (TCKO; $n = 20$) mouse brain sections. (B and C) Percentage of area covered by ApoE immunoreactivity (B) and ApoE immunoreactivity in Clec7a-positive cells (C) was quantified in the hippocampus. (D–F) Representative images from a double stain of Trem2 (red) and Clec7a (green) (D). Percentage of area covered by Trem2 immunoreactivity (E) and ApoE immunoreactivity in Clec7a-positive cells (F) was quantified in the hippocampus. (G and H) Representative images of homeostatic microglia immunostained with P2ry12 in the hippocampus (G). Total P2ry12 immunoreactivity area was analyzed using Imaris (H). Scale bars, 30 μm . Data are expressed as mean \pm SD. One-way ANOVA with Tukey's post hoc test (two-sided) was used for all statistical analysis. * $P < 0.05$, ** $P < 0.01$, *** $P < 0.001$, **** $P < 0.0001$.

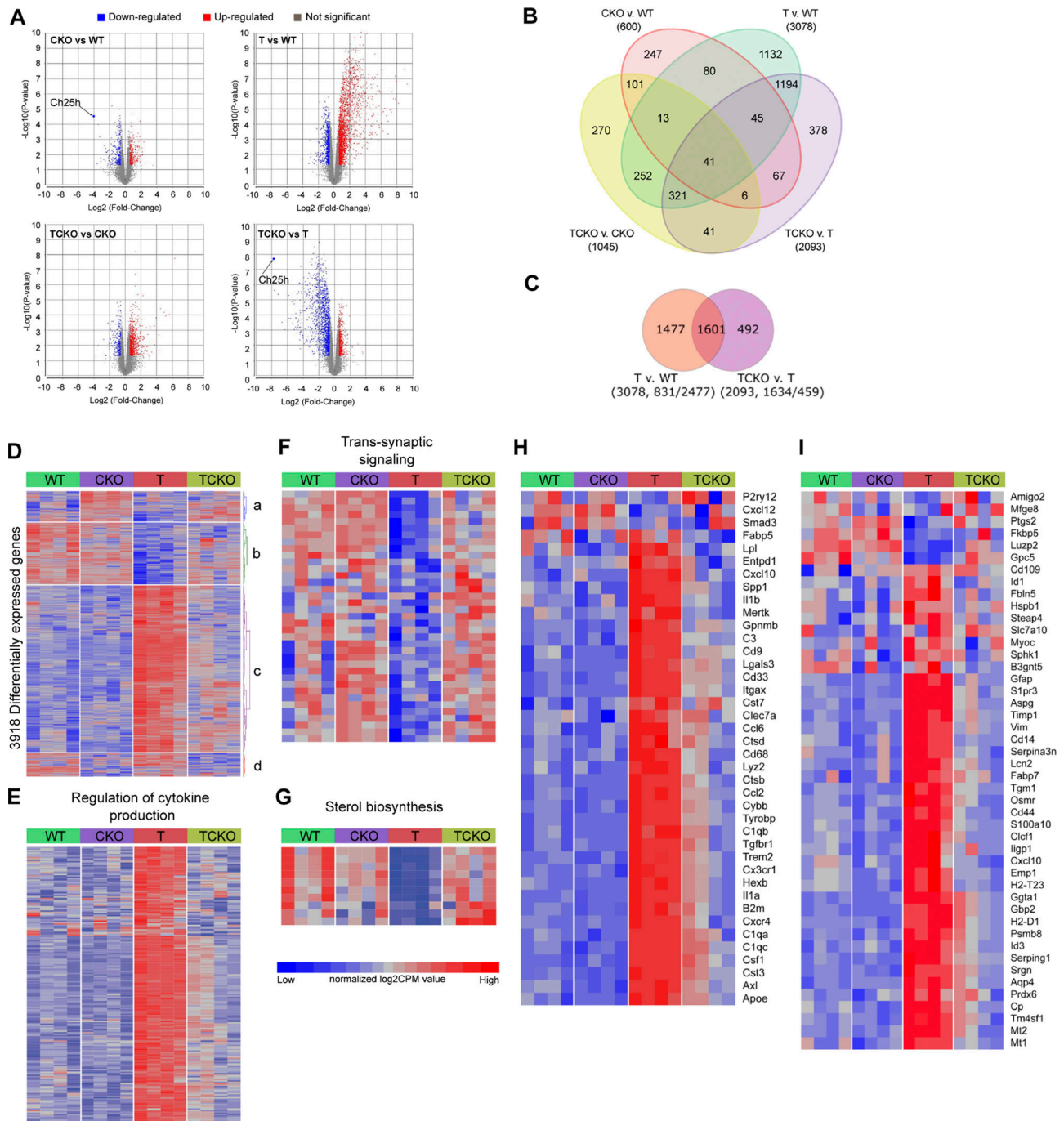


Figure S4. **Transcriptomic changes induced by Ch25h deficiency in PS19 mice.** Volcano plots of significant ($P < 0.05$, $FC > 1.5$) DEGs in the hippocampus of the comparisons CKO versus WT, T versus WT, TCKO versus CKO, and TCKO versus T mice (A). (B and C) Venn diagram (B) showing DEGs in the comparisons CKO versus WT, T versus WT, TCKO versus CKO, and TCKO versus T mice. Venn diagram (C) showing DEGs in the comparisons T versus WT and TCKO versus T. (D) Heatmap of 3,918 DEGs ($P < 0.05$, $FC > 1.5$) in WT, CKO, T, and TCKO mice ($n = 4$ samples per group) showing the effects of Ch25h deficiency and tau transgene. Clusters a and d show DEGs upregulated and downregulated in Ch25h-deficient (CKO and TCKO) groups, respectively. Cluster b shows DEGs downregulated in T and restored in TCKO. (E-G) Cluster c shows DEGs upregulated in T and restored in TCKO. Heatmaps of significant DEGs ($FC > 1.5$, $P < 0.05$) related to the GO terms “regulation of cytokine production” (E), “trans-synaptic signaling” (F), and “sterol biosynthetic process” (G). (H and I) Heatmaps of significant DEGs ($FC > 1.5$, $P < 0.05$) of microglia (H) and astrocyte (I) markers.

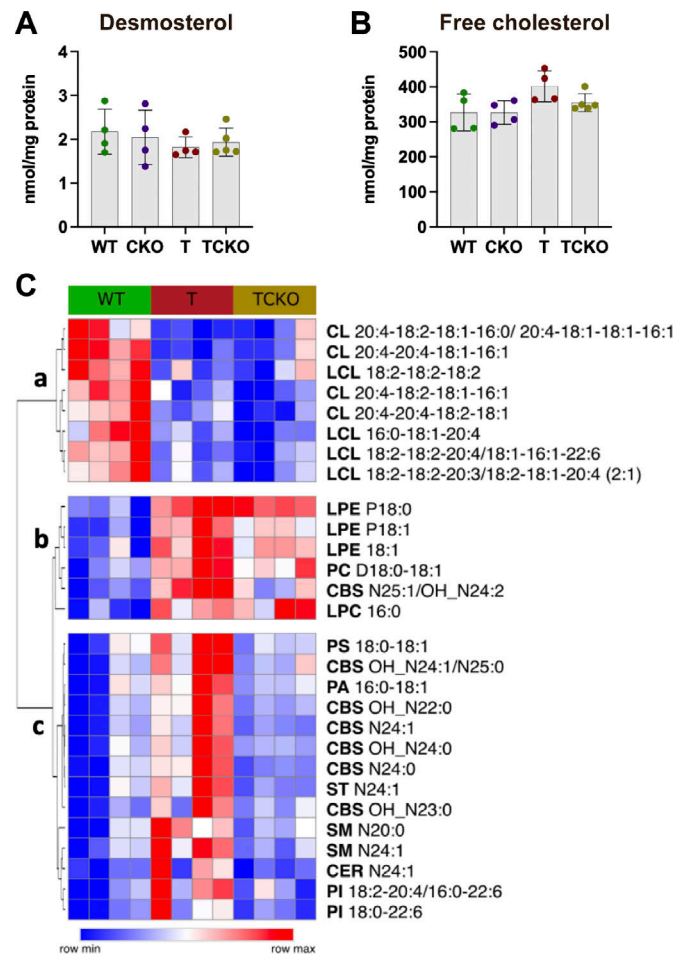


Figure S5. **Ch25h deficiency in PS19 mice modulates levels of specific lipids without affecting free cholesterol levels.** (A and B) Quantification of demosterol (A) and free cholesterol (B) levels in the cortex of 9.5-mo-old WT, CKO, T, and TCKO mice ($n = 4-5$ samples per group). Lipid species were quantified (Table S6) in the cortex of WT, T, and TCKO mice ($n = 4$ per group). One-way ANOVA with Tukey's post hoc test (two-sided) was used for all statistical analysis. (C) Heatmap of lipid species that showed significant differences ($P < 0.05$) between the study groups (row min-max). Clusters a and b show lipids reduced and increased in mice carrying the tau-transgene, respectively. Cluster c shows lipids upregulated in T but restored in TCKO.

Provided online are Table S1, Table S2, Table S3, Table S4, Table S5, Table S6, Table S7, Table S8, Table S9, and Table S10. Table S1 shows demographic information of the human brain tissue samples. Table S2 shows the total number of DEGs. Table S3 lists DEGs. Table S4 lists DEGs showing only the significant DEGs for each comparison (P value < 0.05 and FC of 1.5). Table S5 shows GO term analysis for up- and downregulated genes in T versus WT and TCKO versus T comparisons. Table S6 shows the determination of lipid species in the cortex of WT, T, and TCKO mice by LC/MS. Table S7 shows the summary of the data size of snRNA-seq results. Table S8 shows the integrated average gene expression of cell type-specific markers. Table S9 shows differential gene expression in the microglia cluster. Table S10 shows the relative frequency of the microglia cluster.